European Journal of Radiology xxx (2012) xxx–xxx

Contents lists available at SciVerse ScienceDirect

European Journal of Radiology

journal homepage: www.elsevier.com/locate/ejrad

Assessment of CAD-generated tumor volumes measured using MRI in breast cancers before and after neoadjuvant chemotherapy

Kazuna Takeda[a,1], Shotaro Kanao[a,*], Tomohisa Okada[a,1], Masako Kataoka[a,1], Takayuki Ueno[b,1], Masakazu Toi[b,1], Hiroshi Ishiguro[c,1], Yoshiki Mikami[d,1], Kaori Togashi[a,1]

[a] Department of Diagnostic Imaging and Nuclear Medicine, Kyoto University Graduate School of Medicine, 54 Shogoin Kawaharacho, Sakyoku, Kyoto 606-8507, Japan
[b] Department of Breast Surgery, Kyoto University Graduate School of Medicine, 54 Shogoin Kawaharacho, Sakyoku, Kyoto 606-8507, Japan
[c] Department of Outpatient Oncology Unit, Kyoto University Graduate School of Medicine, 54 Shogoin Kawaharacho, Sakyoku, Kyoto 606-8507, Japan
[d] Department of Diagnostic Pathology, Kyoto University Graduate School of Medicine, 54 Shogoin Kawaharacho, Sakyoku, Kyoto 606-8507, Japan

ARTICLE INFO

Article history:
Received 28 September 2011
Received in revised form 8 December 2011
Accepted 9 December 2011

Keywords:
MRI
Breast cancer
Neoadjuvant chemotherapy
Computer-aided measurement
Inter-observer agreement

ABSTRACT

Objective: To evaluate inter-observer agreement and the predictive value of tumor size measurements using MRI for breast cancer under neoadjuvant chemotherapy (NAC) by comparing the measurements of the longest diameters (LD), total enhanced volumes (TEV) and washout volumes (WOV).
Methods: Thirty-seven female breast cancer patients were prospectively enrolled from August 2008 to October 2010. Two of these patients had locally advanced disease. MRI examinations were acquired within 2 weeks before and after NAC. Interim scans were also conducted in 30 patients. Tumor resection was undertaken within 2 weeks after the cessation of NAC. MRI images were independently measured for LD, TEV and WOV by two experienced radiologists. Inter-observer agreement was evaluated using concordance correlation coefficients (CCCs). Tumor sizes after NAC were evaluated relative to their initial sizes for early prediction of a pathological complete response (pCR).
Results: The CCCs were 0.93 (CI: 0.90–0.95) for LD, 0.98 (CI: 0.97–0.98) for TEV and 0.99 (CI: 0.991–0.996) for WOV. All measurements had high inter-observer agreement, but the CCCs were significantly increased in the aforementioned order ($P < 0.0001$). WOV measured after the completion of chemotherapy had significant discriminating ability ($P = 0.0056$) when evaluated using receiver operating characteristic analysis, and was found to be superior to LD ($P = 0.045$). The average WOV size was significantly smaller in pCR cases than in non-pCR cases ($P = 0.016$).
Conclusion: Computer-aided detection-generated tumor volumes had significantly higher inter-observer concordance than conventional LD measurements. WOV measurements had the highest concordance, and WOV could better predict pCR after NAC at smaller tumor sizes.

1. Introduction

Neoadjuvant chemotherapy (NAC), which is conducted before surgery, is now commonly adopted to treat breast cancer [1]. This therapy was initially indicated for patients with locally advanced or inflammatory breast cancers, but the indication has expanded to include operable breast cancer patients who are not candidates for breast conserving surgery but may get some benefit from tumor volume reduction [2]. Advantages of this therapeutic approach are early treatment of micrometastatic disease, assessment of tumor response to specific chemotherapeutic regimens *in vivo* and analyses of biological markers (e.g. Ki-67, estrogen receptor, progesterone receptor and human epidermal growth factor receptor 2) that may predict the response [3].

Randomized controlled trials comparing NAC and postoperative adjuvant chemotherapy have shown similar survival benefit, and preoperative chemotherapy has allowed more patients to undergo successful breast-conserving treatment [4]. Moreover, pathological complete response (pCR) of primary breast cancer to NAC is a surrogate marker for good outcome [4]. Evaluation of the tumor before surgery has been conducted using modalities including mammography, ultrasound and MRI. MRI is recognized as the most reliable method for the detection of residual tumor after NAC [5–7]. In dynamic MRI, the total enhanced volume (TEV) of a tumor is well visualized, and the enhanced volume with washout volume (WOV)

* Corresponding author. Tel.: +81 75 751 3760; fax: +81 75 771 9709.
E-mail addresses: kazunat@kuhp.kyoto-u.ac.jp (K. Takeda), kanaos@kuhp.kyoto-u.ac.jp (S. Kanao), tomokada@kuhp.kyoto-u.ac.jp (T. Okada), makok@kuhp.kyoto-u.ac.jp (M. Kataoka), takayuki@kuhp.kyoto-u.ac.jp (T. Ueno), toi@kuhp.kyoto-u.ac.jp (M. Toi), hishimd@kuhp.kyoto-u.ac.jp (H. Ishiguro), mika@kuhp.kyoto-u.ac.jp (Y. Mikami), ktogashi@kuhp.kyoto-u.ac.jp (K. Togashi).
[1] Tel.: +81 75 751 3760; fax: +81 75 771 9709.

0720-048X/$ – see front matter © 2011 Elsevier Ireland Ltd. All rights reserved.
doi:10.1016/j.ejrad.2011.12.013

is known to have high activity [8]. These parameters might be predictors of pCR, as well as the most used criteria, namely longest diameter (LD).

For the evaluation of tumor response to NAC, Response Evaluation Criteria in Solid Tumors (RECIST) [9] is mainly used, and the LD of a residual tumor is measured. There are some studies on measurement in two orthogonal directions, but no difference has been reported as compared with the LD method [10]. The RECIST criteria were validated in more than 4000 patients, and are currently being considered as the method of choice for the morphological assessment of tumor response to a given treatment. However, three-dimensional (3D) volumetry is reported to have higher sensitivity to changes in the tumor size, especially in cases of irregular tumor morphology or multiple tumor foci [11].

There are some variations in measurement reproducibility in the volumetry of tumors under chemotherapy both using CT [12] or MRI [13]. Such observations necessitate semi-automated segmentation and measurement of tumors visualized by MRI using a workstation [11,14], although there still remain some human factors. Semi-automated computer-assisted measurements of MRI were more accurate than those conducted manually [15]. Manual volumetry of residual breast cancer using MRI is reported to better correlate with prognosis than LD measurements [16]. However, inter-observer agreement of tumor size measurement has been investigated considerably less frequently using semi-automated methods than using the conventional method.

Therefore, we hypothesized that computer-aided semi-automated volumetry of breast cancer using MRI would attain higher inter-observer agreement in size evaluation as compared with the conventional LD measurement. We also investigated if tumor size reduction could predict pCR during and after NAC by measuring the LD, TEV and WOV.

2. Materials and methods

2.1. Patients and therapeutics

This study was approved by our Institutional Review Board, and informed consent was obtained by all subjects enrolled. Female patients newly diagnosed as having breast cancer at our hospital from August 2008 to October 2010 were considered. Two of these patients had locally advanced disease. Among the patients, those who had MRI examinations within 2 weeks before the first chemotherapy, and within 2 weeks after NAC and before tumor resection, were prospectively enrolled in the study. Thirty-seven females with an average age of 51 years (range, 30–78 years) were enrolled. Forty-six MRI examinations were also conducted during NAC. There were 120 MRI examinations available in total.

All patients were treated with NAC and surgically resected thereafter at our hospital. The final therapy was decided by the patient with informed consent after discussion with breast surgeons and a medical oncologist. The basic regimen of NAC was a combination of docetaxel (75 mg/m^2) and cyclophosphamide (600 mg/m^2) for 3–6 cycles administered every 3 weeks. No endocrine therapy was carried out.

2.2. MRI protocol

MRI evaluation was conducted at least twice before and after neoadjuvant chemotherapies using the same protocol. Many patients had one to three MRI examinations during the NAC periods. MRIs were acquired using a 3T scanner (Magnetom Trio Tim; Siemens Medical Solutions, Erlangen, Germany) with a breast-dedicated four-channel coil (Invivo, Gainesville, FL, USA). After obtaining axial T2-weighted, T1-wighted and diffusion-weighted images, fat-suppressed T1-weighted dynamic images were acquired once before and three times at 0–1, 1–2 and 5–6 min after gadolinium injection. The whole breasts were scanned in high temporal resolution for 1 min (3D-VIBE: TR/TE 3.8/1.48 ms, FA 15 and FOV 330 mm × 330 mm, matrix 448 × 461, 2.5 mm thickness, 60 slices) in axial orientation. At 2–5 min, a high-resolution scan was conducted (3D-VIBE: TR/TE 4.2/1.5 ms, FA 15, FOV 330 mm × 330 mm, matrix 448 × 412 and 176 slices of thickness 0.8 mm) in coronal orientation. Infused gadolinium contrast materials were either Gadoteridol (ProHance, Eisai Inc., Tokyo, Japan) or Gadodiamide (Omniscan, Daiichi-Sankyo Inc., Tokyo, Japan) at a dose of 0.2 ml/kg power injected at a speed of 2.0 ml/s and flashed with 20 ml of saline at the same rate.

2.3. Image analysis

All MRI examinations were processed using BreVis (Siemens, Erlangen, Germany), a commercially available computer-aided detection system. This system incorporates four MRI series into its calculations: one pre-contrast T1-weighted series and three post-contrast T1-weighted series. Tumors were measured manually for LD or semi-automatically for TEV and WOV, independently by two experienced radiologists (S.K. and K.T., with 10 and 4 years' experience in the breast MRI examination, respectively). The LD was measured on multi-planar reconstructed images that presented the largest extent of the tumor (Fig. 1A). The TEV was measured by placing the smallest cube that circumscribed the enhanced tumor, with equal to or more than 50% signal increase, mainly on the second post-contrast images (Fig. 1B). The WOV was calculated by further selecting enhanced areas with more than 100% signal increase and signal reduction by more than or equal to 10% on delayed post-contrast T1-weighted images (Fig. 1C). Enhancements in an area where a tumor had existed before therapy were considered to indicate a residual tumor. Central necrosis, if any, was enclosed [14]. Enhancements at other areas were considered non-specific, except when they had definite malignant morphology or a dynamic enhancement pattern. If the lesion consisted of multiple adjacent abnormalities, the maximum dimension was not the sum of their diameters, but a single measurement encompassing the lesions that were farthest apart [7]. To confirm the processes, both evaluators together measured 10 training cases that were not enrolled in this study.

2.4. Pathological analysis

The specimens were sectioned at 5-mm intervals perpendicular to the longest axis of a specimen. After all sections were formalin-fixed and paraffin-embedded, they were examined for residual cancer. Assessments were made using conventional hematoxylin–eosin stained sections, and immunohistochemical staining of cytokeratin was also conducted using monoclonal anti-cytokeratin antibody AE1/AE3 (DAKO Cytomation, Glostrup, Denmark) in 16 patients, because assessment of residual cancer cells was difficult. Pathological CR was defined as no residual invasive tumor in the specimen.

2.5. Statistical analysis

Inter-observer agreement for the measurements of the two radiologists was calculated using concordance correlation coefficients (CCCs) [17] for the three measurement methods of LD, TEV and WOV, and their differences was evaluated. In order to investigate if residual tumor size measured on MR images during and after NAC can predict pCR, receiver operating characteristic (ROC) curve analysis was conducted for the three methods. The average tumor sizes of the pCR and non-pCR groups before, during and after NAC

Please cite this article in press as: Takeda K, et al. Assessment of CAD-generated tumor volumes measured using MRI in breast cancers before and after neoadjuvant chemotherapy. Eur J Radiol (2011), doi:10.1016/j.ejrad.2011.12.013

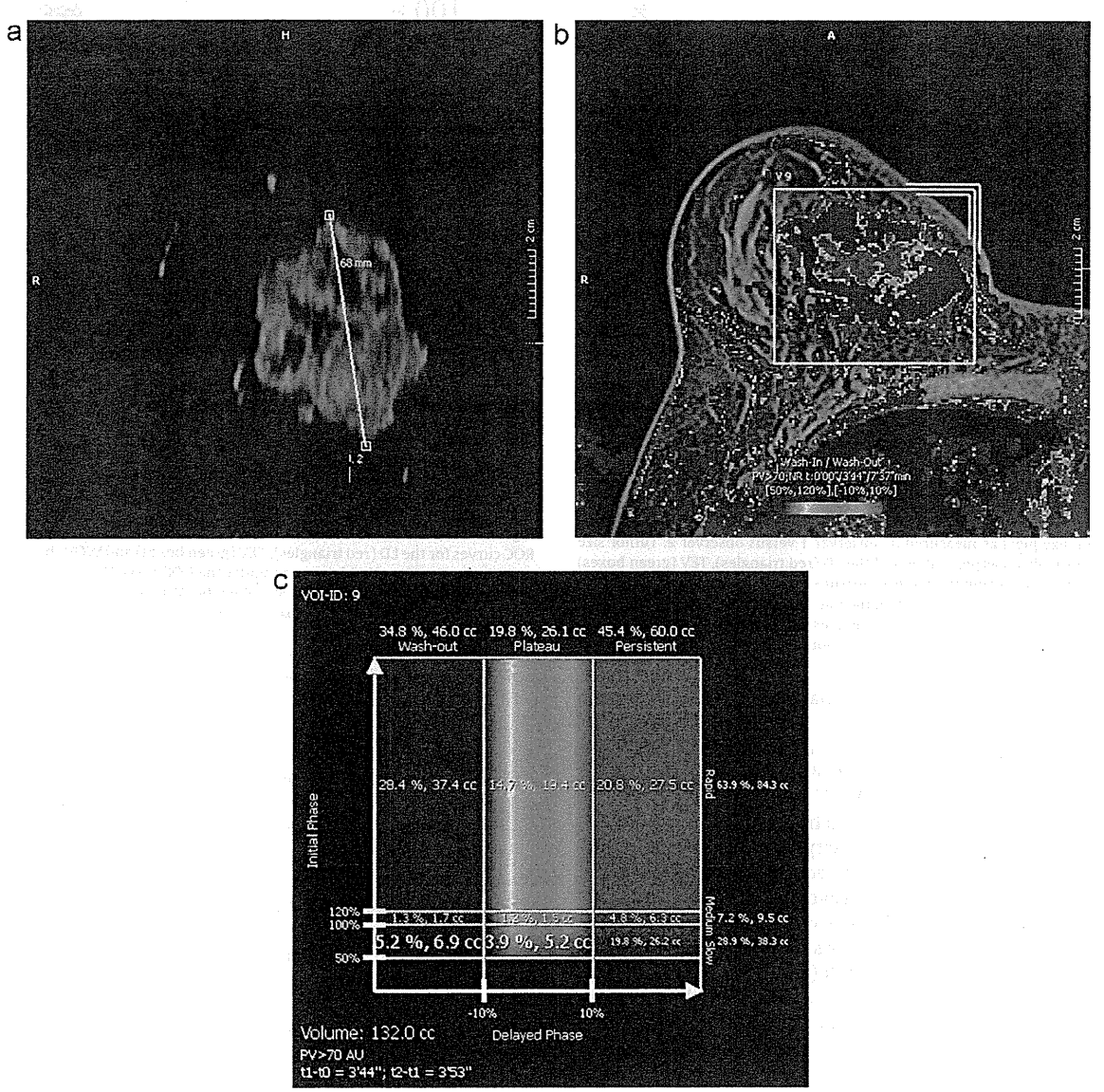

Fig. 1. A 57-year-old woman with right breast cancer. (A) The longest diameter (LD) was measured on a coronal plane reformatted using multi-planner reconstruction. (B) The total enhanced volume (TEV) was measured by setting a rectangular region of interest that circumscribed a tumor that exhibited a signal increase, by more than or equal to 50% on the early phase images. (C) The enhanced volume with washout pattern (WOV) was defined as areas with a signal increase of more than or equal to 100% on the early phase images, and a signal decrease of more than or equal to 10% on the delayed phase images.

were also compared. A P value of less than 0.05 was considered statistically significant. All statistical analyses were carried out using MedCalc (MedCalc Software, Mariakerke, Belgium).

3. Results

The CCC values were 0.93 (CI: 0.90–0.95), 0.98 (CI: 0.97–0.98) and 0.99 (CI: 0.991–0.996) for the LD, TEV and WOV, respectively. All measurements had high inter-observer agreement, but the CCCs significantly increased in the order of LD, TEV and WOV ($P < 0.0001$, Tables 1 and 2, Fig. 2).

Among 37 cases in total, 11 cases were found to be pCR and the other 26 cases were not. In these 11 patients, multiple adjacent abnormalities were found in nine. In all cases, 30 patients had MRI examinations during NAC and there were 11 pCR cases. No significant differences were found in age ($P = 0.79$), gender, initial LD

Table 1
Inter-observer agreement analysis using the CCC.

	CCC	CI
LD	0.930	0.901–0.950
TEV	0.977	0.968–0.983
WOV	0.994	0.991–0.996

CCC, concordance correlation coefficient; CI, confidence interval; LD, longest diameter; TEV, total enhanced volume; and WOV, enhanced volume with washout pattern.

Table 2
Comparison among CCCs.

	Z	P
TEV vs. LD	4.31	<0.0001
WOV vs. TEV	5.17	<0.0001
WOV vs. LD	9.48	<0.0001

CCC, concordance correlation coefficient; LD, longest diameter; TEV, total enhanced volume; and WOV, enhanced volume with washout pattern.

Please cite this article in press as: Takeda K, et al. Assessment of CAD-generated tumor volumes measured using MRI in breast cancers before and after neoadjuvant chemotherapy. Eur J Radiol (2011), doi:10.1016/j.ejrad.2011.12.013

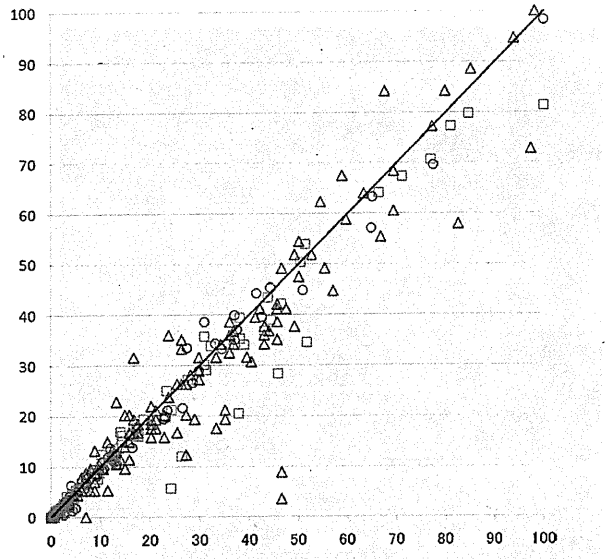

Fig. 2. Tumor size plots as measured by observer 1 versus observer 2. Tumor size values were normalized as percentages of the LD (red triangles), TEV (green boxes) and WOV (blue circles) using the largest measured sizes by either observer 1 or 2. The plot shows decreasing deviation from the line of perfect agreement (black line) in the order of the LD, TEV and WOV. LD, longest diameter; TEV, total enhanced volume; and WOV, enhanced volume with washout pattern.

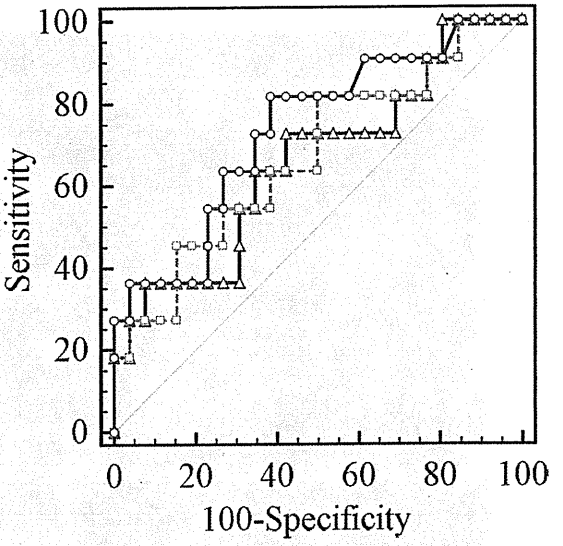

Fig. 3. Differentiation of non-pCR and pCR after completion of chemotherapy using ROC curves for the LD (red triangles), TEV (green boxes) and WOV (blue circles). The WOV had a significantly higher area under the ROC curve ($P = 0.0056$) with a sensitivity of 81.8% and specificity of 61.5%, when the WOV was reduced to equal to or less than 46.3% of the initial size. Comparisons of the ROC curves indicated that the WOV had a significantly larger area under the curve than the LD ($P = 0.045$). ROC, receiver operating characteristic; LD, longest diameter; TEV, total enhanced volume; WOV, enhanced volume with washout pattern; and pCR, pathological complete response.

($P = 0.68$), initial TEV ($P = 0.95$) and initial WOV ($P = 0.63$) between the pCR and non-pCR groups.

ROC curve analysis did not reveal any significant predictive capability in relation to pCR in terms of the tumor size measurements during NAC. However, the WOV measurements after NAC were found to have significant predictive capability ($P = 0.0056$) with a sensitivity of 81.8 and a specificity of 61.5, using size reduction criteria of less than 46.3% compared with the initial size. The WOV was reduced to 35% and 59% on average for pCR and non-pCR groups, respectively, and the difference was statistically significant ($P = 0.016$) (Table 3). ROC curve analysis found that the LD had no significant capability in predicting pCR ($P = 0.096$), as was also the case with the TEV ($P = 0.065$). WOV had a higher capability in predicting pCR than the LD ($P = 0.045$), but not when compared with the TEV ($P = 0.33$) using ROC curve comparisons (Fig. 3).

4. Discussion

In the present study, all the three measurement methods, namely LD, TEV and WOV, were shown to have high inter-observer agreement. However, as compared with the conventional method for the measurement of the LD, TEV and WOV, measurements that use semi-automated volume calculations had significantly higher CCC values. As has been reported previously, semi-automated analysis contributed to increased reproducibility, but regions of interest had to be defined by the individual carrying out the measurement and this caused some residual variations, which is considered inevitable. In WOV measurement, the washout pattern, which is known to be highly specific to the tumor, is automatically defined by the software. This probably contributed to increasing inter-observer agreement. On the other hand, the choice of the slice thickness used to measure the LD can differ among investigators, and this results in larger variances than found using other methods.

Table 3
A comparison of WOVs between non-pCR and pCR cases after completion of chemotherapy.

	Non-pCR	pCR
Number of patients	26	11
Mean size after NAC (%)	59.0	35.1
95% CI	48.5–70.0	16.9–53.2

CI, confidence interval; pCR, complete response; and WOV, enhanced volume with washout pattern.

The capability of tumor measurements in predicting pCR after NAC was significantly higher only in the case of the WOV measurements. Volume measurement has been reported to better correlate to pathological outcome than measurement of the largest tumor length [16]. In our study, more detailed investigations were carried out and confirmed the significant superiority of WOV measurements in terms of the reproducibility and capability of predicting pCR, as compared with other methods including conventional LD. In the present study, the TEV was defined as enhanced areas with more than or equal to 50% early signal increases, and the WOV as enhanced areas with more than or equal to 100% early signal increase, and more than or equal to 10% signal decrease on delayed post-contrast T1-weighted images. Different thresholds may give different diagnostic capability, and further studies might be required to justify the thresholds.

Recent studies suggest that the RECIST method may have limited value in evaluation, because small changes in tumor sizes are difficult to detect using this method [18,19] In pulmonary metastases, automatic volumetry has higher intra- and inter-observer agreement than the RECIST method of measuring LD, and it enables more accurate evaluations of the therapeutic outcome of chemotherapies [19]. This finding has also been reported for breast cancer [15]. However, the method involving volumetry has not yet been standardized, and there is only limited availability [9]. The latter limitation is gradually being diminished by the recent introduction of various kinds of computer-aided measurement programs, and there will be more to come [20]. Semi- or fully automated volumetry may substitute RECIST in near future.

The present study had several limitations. The software used for volumetry could only define rectangular ROIs, which may have contained some non-tumorous tissues. This may have contributed to degradation of the discrimination between pCR and non-pCR.

Please cite this article in press as: Takeda K, et al. Assessment of CAD-generated tumor volumes measured using MRI in breast cancers before and after neoadjuvant chemotherapy. Eur J Radiol (2011), doi:10.1016/j.ejrad.2011.12.013

Another limitation was that although all of the tumors were invasive ductal carcinoma, there were differences among tumors in terms of the modified Scarff–Bloom–Richardson grades and hormonal receptor types. There were also some variations in the chemotherapy regimens. These were customized for each individual patient and the treatment periods were not the same, which is somewhat inevitable in clinical cases.

5. Conclusion

Semi-automated measurements of tumor volume had significantly higher inter-observer agreement than conventional measurement of LD in breast cancer. Among these measurements, the WOV could predict pCR at a significantly higher level than the LD. Semi-automated measurement will introduce more reliable evaluations into clinical practice.

Conflict of interest

No authors have any financial relationship with any organization related to this study.

References

[1] Tardivon A, Ollivier L, El Khoury C, Thibault F. Monitoring therapeutic efficacy in breast carcinomas. Eur Radiol 2006;16(11):2549–58.
[2] van der Hage JA, van de Velde CJ, Julien JP, Tubiana-Hulin M, Vandervelden C, Duchateau L. Preoperative chemotherapy in primary operable breast cancer: results from the European Organization for Research and Treatment of Cancer trial 10902. J Clin Oncol 2001;19(22):4224–37.
[3] Yerushalmi R, Woods R, Ravdin PM, Hayes MM, Gelmon KA. Ki67 in breast cancer: prognostic and predictive potential. Lancet Oncol 2010;11(2):174–83.
[4] Wolmark N, Wang J, Mamounas E, Bryant J, Fisher B. Preoperative chemotherapy in patients with operable breast cancer: nine-year results from National Surgical Adjuvant Breast and Bowel Project B-18. J Natl Cancer Inst Monogr 2001;(30):96–102.
[5] Balu-Maestro C, Chapellier C, Bleuse A, Chanalet I, Chauvel C, Largillier R. Imaging in evaluation of response to neoadjuvant breast cancer treatment benefits of MRI. Breast Cancer Res Treat 2002;72(2):145–52.
[6] Takeda K, Kanao S, Okada T, et al. MRI evaluation of residual tumor size after neoadjuvant endocrine therapy vs. neoadjuvant chemotherapy. Eur J Radiol 2011.
[7] Rosen E, Blackwell K, Baker J, et al. Accuracy of MRI in the detection of residual breast cancer after neoadjuvant chemotherapy. AJR Am J Roentgenol 2003;181(5):1275–82.
[8] Kuhl C, Mielcareck P, Klaschik S, et al. Dynamic breast MR imaging: are signal intensity time course data useful for differential diagnosis of enhancing lesions? Radiology 1999;211(1):101–10.
[9] Eisenhauer EA, Therasse P, Bogaerts J, et al. New response evaluation criteria in solid tumours: revised RECIST guideline (version 1.1). Eur J Cancer 2009;45(2):228–47.
[10] James K, Eisenhauer E, Christian M, et al. Measuring response in solid tumors: unidimensional versus bidimensional measurement. J Natl Cancer Inst 1999;91(6):523–8.
[11] Partridge SC, Gibbs JE, Lu Y, et al. MRI measurements of breast tumor volume predict response to neoadjuvant chemotherapy and recurrence-free survival. AJR Am J Roentgenol 2005;184(6):1774–81.
[12] Sohaib SA, Turner B, Hanson JA, Farquharson M, Oliver RT, Reznek RH. CT assessment of tumour response to treatment: comparison of linear, cross-sectional and volumetric measures of tumour size. Br J Radiol 2000;73(875):1178–84.
[13] Martincich L, Montemurro F, De Rosa G, et al. Monitoring response to primary chemotherapy in breast cancer using dynamic contrast-enhanced magnetic resonance imaging. Breast Cancer Res Treat 2004;83(1):67–76.
[14] Kubben PL, Postma AA, Kessels AG, van Overbeeke JJ, van Santbrink H. Intraobserver and interobserver agreement in volumetric assessment of glioblastoma multiforme resection. Neurosurgery 2010;67(5):1329–34.
[15] Partridge SC, Heumann EJ, Hylton NM. Semi-automated analysis for MRI of breast tumors. Stud Health Technol Inform 1999;62:259–60.
[16] Akazawa K, Tamaki Y, Taguchi T, et al. Potential of reduction in total tumor volume measured with 3D-MRI as a prognostic factor for locally-advanced breast cancer patients treated with primary chemotherapy. Breast J 2008;14(6):523–31.
[17] Lin LI. A concordance correlation coefficient to evaluate reproducibility. Biometrics 1989;45(1):255–68.
[18] Ratain MJ, Eckhardt SG. Phase II studies of modern drugs directed against new targets: if you are fazed, too, then resist RECIST. J Clin Oncol 2004;22(22):4442–5.
[19] Marten K, Auer F, Schmidt S, Kohl G, Rummeny EJ, Engelke C. Inadequacy of manual measurements compared to automated CT volumetry in assessment of treatment response of pulmonary metastases using RECIST criteria. Eur Radiol 2006;16(4):781–90.
[20] Demartini WB, Lehman CD, Peacock S, Russell MT. Computer-aided detection applied to breast MRI: assessment of CAD-generated enhancement and tumor sizes in breast cancers before and after neoadjuvant chemotherapy. Acad Radiol 2005;12(7):806–14.

Please cite this article in press as: Takeda K, et al. Assessment of CAD-generated tumor volumes measured using MRI in breast cancers before and after neoadjuvant chemotherapy. Eur J Radiol (2011), doi:10.1016/j.ejrad.2011.12.013

Tohoku J. Exp. Med., 2011, 224, 1-5

Review

Clinical Applications of Sentinel Lymph Node Biopsy in Ductal Carcinoma *in situ* of the Breast: A Dilemma

Yu Tang,[1,*] Fei Xu,[1] Kaishan Tao,[2,*] Niansong Qian[3,4] and Masakazu Toi[4]

[1]Department of Ultrasound, PLA 302 Hospital, Beijing, P.R. China
[2]Department of Hepatobiliary Surgery, Xijing Hospital, Fourth Military Medical University, Xi'an, P.R. China
[3]Department of Hepatobiliary Surgery, PLA General Hospital, Beijing, P.R. China
[4]Department of Breast Surgery, Graduate School of Medicine, Kyoto University, Kyoto, Japan

Breast cancer is the fifth most common cause of cancer deaths in the world, which often spreads first to the axillary lymph nodes (ALN) from the primary tumor. ALN helps clinician stage breast cancer. In addition, it is one of the key prognostic factors for patients with invasive breast cancer. The sentinel lymph node (SLN) is defined as the first regional lymph node to receive lymphatic fluid from a malignant tumor. As a result, it seems possible to assess the complete nodal status with sentinel lymph node biopsy (SLNB), which is attractive and reliable approach for identifying lymph node metastasis. Ductal carcinoma in situ (DCIS) is the most common type of non-invasive breast cancer. However, the role of SLNB in DCIS is controversial because DCIS does not cause invasion and metastasis theoretically. In this review, clinical applications of SLNB in DCIS will be discussed. The potential benefit of accurately upstaging patients with DCIS and the minimal invasiveness of SLNB justify use of SLNB in selected high-risk DCIS patients. At least DSIS with microinvasion, have DCIS of sufficient extent on mammography or MRI, or indicated invasive or microinvasive focus by final histological examination, are recommended for SLNB. Moreover, large randomized trials to evaluate the usefulness of SLNB in DCIS patients after long-term follow-up on local control and survival are required for further evaluation.

Keywords: breast cancer; ductal carcinoma in situ; axillary lymph node; sentinel lymph node biopsy; microinvasion
Tohoku J. Exp. Med., 2011, **224** (1), 1-5.

Breast cancer is the second most common type of non-skin related cancer and the fifth most common cause of cancer deaths in the world. Late onset diagnosis, resistance to anti-tumor therapy, tumor size, pathological type, and axillary lymph node (ALN) metastases indicate poor prognosis of breast cancer patients. The sentinel lymph node (SLN) is defined as the first regional lymph node to receive lymphatic fluid from a malignant tumor. As a result, it seems possible to assess the complete nodal status with sentinel lymph node biopsy (SLNB), which is attractive and reliable approach for identifying lymph node metastasis. Recently the standard of care in many countries (such as Japan and China) has shifted from full ALN dissection (ALND) to SLNB. Ductal carcinoma in situ (DCIS) of the breast is defined as a proliferation of neoplastic epithelial cells within the duct that is normally surrounded by myoepithelial cells and an intact basement membrane. At present, the treatment of DCIS comprises wide local excision or mastectomy according to its extent. Theoretically, DCIS does not cause ALN metastasis. However, some DCIS patients may be found to harbor occult invasive breast cancer following their surgical procedure. SLNB represents a minimally invasive approach to the surgical management of the axilla and has become a standard of care for patients with invasive breast cancer. However, its role in the surgical management of DCIS is still an open question. In the present paper, clinical applications of SLNB in DCIS will be discussed.

Ductal carcinoma in situ (DCIS)

DCIS is a heterogeneous, unicentric precursor of invasive breast cancer, which is frequently identified through core needle biopsy and mammographic breast screening programs (Espina et al. 2010). Theoretically, DCIS does not cause invasion and metastasis. However, more and more researchers indicate that DCIS is a lesion with maligned potential and may progress to invasive breast cancer. Researchers have suggested that pure DCIS and DCIS with microinvasion (DCISM) are distinct entities. As mentioned by Maass et al (Maass et al. 2009), tumor-infiltrated

Received December 28, 2010; revision accepted for publication April 1, 2011. doi: 10.1620/tjem.224.1
* Yu Tang and Kaishan Tao contributed equally to this work.
Correspondence: Niansong Qian, M.D., Ph.D., Department of Hepatobiliary Surgery, Chinese PLA General Hospital, 28 Fuxing Road, Beijing 100853, P.R. China.
e-mail: kyotomed@foxmail.com

resection margins, residual microcalcification, treatment by local excision alone, age less than 35 years, tumor size, histological grading, and microinvasion are associated with high risks of local recurrence of DCIS. According to the review by Sakorafas et al. (Sakorafas et al. 2008), high expression of COX2 and/or Ki67, P53 mutation, c-erB2 amplification, presence of necrosis, high nuclear grade and EP/PgR negative can predict biological behavior of DCIS. A variety of different definitions have been used for DCISM, including DCIS showing focal microinvasion below the basement membrane or limited microscopic stromal invasion but not invading more than 10% of the surface of the histological sections examined, the maximal extent of invasion is not more than 2mm or comprising < 10% of the tumor with 90% of DCIS and a few single infiltrating tumor cells (from 1 to 15) (DCISM type 1) or a few infiltrating tumor cell clusters (DCISM type 2) (Bianchi and Vezzosi 2008). In addition, risk factors mentioned above may be related to an increased chance of axillary involvement.

Sentinel lymph node biopsy (SLNB)

The SLN is defined as the first regional lymph node to receive lymphatic fluid from a malignant tumor (Yeung et al. 2001). As a result, it seems possible to assess the complete nodal status with SLNB. In addition, the significant morbidity of ALND makes this less invasive approach more attractive and reliable (Berveiller et al. 2010). Gipponi et al. (2004) performed histopathologic validation of the SLNB in 334 early-stage breast cancer patients and showed that the prediction of ALN status was remarkably satisfying (93-95% sensitivity and 100% specificity). These findings suggested that the SLNB could accurately predict ALN status. Nowadays, SLNB is well accepted and recommended as the standard method for early-stage breast cancer patients.

Importantly, the false-negative rate of evaluation of SLN status for metastatic spread is very small. Veronesi et al. observe 953 patients who did not undergo ALND after negative SLNB for the appearance of overt axillary metastases with a median follow-up of 38 months. Only 3 cases of overt axillary metastases were found among these patients and the 5-year overall survival rate of the whole series was 98% (Veronesi et al. 2005). However, the role of repeat SLNB is not clear yet in patients with a local recurrence after a negative SLNB. It could also be related to the level of experience of the various surgeons from different hospitals or to different techniques used for injection (Derkx et al. 2010).

The role of SLNB in DCIS

As mentioned above, SLNB is indicated to patients with invasive breast cancer to determine prognosis and to guide adjuvant treatment decisions. However, its role in DCIS is still controversial. Theoretically, SLNB is not recommended for patients with DCIS patients because DCIS does not cause axillary metastasis. However, about 15% of patients who are preoperatively diagnosed with DCIS on core needle biopsy are found to have a co-existing invasive carcinoma. Thus, these patients may benefit from axillary staging (Virnig et al. 2010). Instead of ALND, SLNB might be an option in cases of widespread DCIS and the clinical suspicion of occult microinvasion and/or micrometastasis.

Experience from published retrospective studies

Retrospective studies have been widely used for investigating the role of SLNB in DCIS (Table 1). Sakr et al. (2006) reported a series of 128 patients; 4 of the 128 patients upstaged to invasive carcinoma had metastatic SLN, 10% of the pure DCIS patients with SLNB and 7% of the DCISM patients with SLNB had axillary micrometastasis. So they indicated that SLNB could not only help to avoid under or over treatment of patients with diffuse or palpable DCIS, DCISM, or casting-type calcifications programmed for mastectomy, but also be recommended for DCIS harboring a potential of upstaging to invasive carcinoma. Next, the same group analyzed the data of 195 patients who were initially diagnosed with DCIS. Of the 195 patients with pure DCIS, 31 patients were found to have invasive disease upon final histology and sixteen patients had a positive SLNB (7 in pure DCIS, 2 in DCISM, and 7 in invasive cancer, respectively). Noticeably, all 7 positive SLNB patients in pure DCIS had a tumor size of more than 30 mm. Univariate analysis results indicated that DCISM or large DCIS were one of the high risks of invasive carcinoma after final histologic examination. They further confirmed that SLNB should be performed in order to detect underlying invasive disease and to spare patients a second operating time (Sakr et al. 2008). Another retrospective study indicated that DCIS patients who were planned for mastectomy or who had DCIS size more than 5 cm should perform SLN dissection (Yi et al. 2008). van la Parra la et al. also showed that SLNB had to be considered in the case of a preoperative diagnosis of grade III DCIS or a grade II DCIS with comedo necrosis and DCISM (van la Parra et al. 2008). Similar results were also reported by Moore et al. (2007). Murphy et al. (2008) recommended SLNB in all patients undergoing mastectomy for DCIS or DCISM, although their results showed that positive SLNB in patients with DCIS or DCISM was not associated with higher risk of local or distant recurrence. In a recent retrospective study, similar results were found that SLNB appeared justified in DCIS due to the high rate of underestimation of invasive carcinoma by core needle biopsy diagnosis in their study (Doyle et al. 2009). However, Tada et al. (2010) and Takács et al. (2009) believed SLNB could safely be omitted due to the low rate of SLN metastasis in patients with pure DCIS. Polom et al. (2009) analyzed 183 patients that underwent SLNB from 2000 to 2005. They also agreed that SLNB as a diagnostic tool in DCIS remained controversial as the number of ALN micrometas-

Table 1. Retrospective studies on the role of SLNB in DCIS.

Autor	Years	Cases include in the study	SLN biopsy	Patients with positive SN	Mapping	detected by
Sakr et al	2006	128	53	5	radiotracer	IHC
Sakr et al	2008	80	80	9	radiocolloids	HE, IHC
Yi et al	2008	624	624	40	radiotracer, vital dye	HE, IHC
van la Parra et al	2008	51	51	10	radiotracer, vital dye	HE, IHC
Moore et al	2007	2,136	470	43	blue dye	HE, IHC
Murphy et al	2008	322	322	29	N/A	HE, IHC
Doyle et al	2009	145	145	7	radiotracer, vital dye	HE, IHC
Tada et al	2010	255	255	1	radiotracer	HE
Takács T et al	2009	57	48	0	radiotracer	HE, IHC
Polom et al	2009	261	183	10	radiotracer	HE

Table 2. Prospective studies on the role of SLNB in DCIS.

Autor	Years	Cases include in the study	SLN biopsy	Patients with positive SN	Mapping	detected by
Collado et al	2008	43	N/A	3	N/A	HE
Wilkie et al	2005	675	675	49	radiotracer, vital dye	HE, IHC
Intra et al	2008	854	854	12	radiotracer	HE, IHC
Moran et al	2007	470	470	43	radiotracer, vital dye	HE
Intra et al	2003	223	223	7	radiotracer	HE, IHC
Mittendorf et al	2005	85	85	9	radiotracer	HE, IHC

tases cases is minuscule (Polom et al. 2009). A recently meta-analysis showed a higher incidence of SLN metastases in patients with a preoperative diagnosis of DCIS when compared with a postoperative diagnosis (7.4% versus 3.7%). This significant difference indicated that patients with a preoperative diagnosis of DCIS should be considered for SLNB. However, further efforts are still required (Ansari et al. 2008).

Experience from published prospective studies

Several prospective studies have also been performed to evaluate the role of SLNB on DCIS (Table 2). Collado et al. (2010) reported their experiment on 65 DCIS patients. Definitive histologic study of the resected breast tumor revealed 43 cases of DCIS, 15 of ductal invasive carcinoma and 7 microinvasive tumors. In confirmed DCIS, only 6.9% of SLN were positive, 28.5% in microinvasive carcinoma and 40% in invasive carcinoma were positive (Collado et al. 2010). One of the largest prospective comparative series (675 patients) was presorted by Wilkie et al. (2005). Of all, 613 patients were with DCIS and 62 patients were with DCISM. Among these patients, 55 patients with DCIS and 11 patients with DCISM were upstaged. Forty-nine of 675 patients had positive SLN and 22 had invasive carcinoma or DCISM on final histology. Of notice, microinvasion predicted patients at higher risk for invasive carcinoma. So they recommend SLNB should be performed in selective patients who are undergoing mastectomy for DCIS, patients who have DCISM, patients who have high-grade DCIS at the time of biopsy, and patients who have a mass by mammography. Intra et al. (2003) suggested that SLNB should not be considered a standard procedure in all patients with DCIS because of the low prevalence of metastases. It could be considered in patients with DCIS undergoing mastectomy, in whom there exists a higher risk of harboring an invasive component using definitive histologic features, like large solid tumors or diffuse or multicentric microcalcifications. Similar results were observed in other studies (Moran et al. 2007; Intra et al. 2008). They also indicated that SLNB should be performed on selected high-risk DCIS patients and not be performed routinely for all patients with an initial diagnosis of DCIS. However, there are still different opinions. Mittendorf et al. (2005) studied the role of SLNB in their prospective series of 85 patients who were initially diagnosed with DCIS by biopsy diagnosis. In their investigation, 20% of patients with a core biopsy diagnosis of DCIS were upstaged to invasive disease. So they advocated performing SLNB on all patients with a core biopsy diagnosis of DCIS due to the high rate of underestimation.

Identification of subgroup of DCIS patients who may benefit from SLNB

The relationship between DCIS and invasive breast cancer remains unclear. This relationship can be found in the similarity of risk factors for both the incidence of the diseases and their similar responses to treatment. In fact, 2% to 20% of patients with a core biopsy diagnosis of DCIS were upstaged to invasive disease, depending on the

selection criteria and analytical methods. Clearly, such differences must lead to a reexamination for whom with a preoperative diagnosis of DCIS. SNLB, therefore, is indicated at least in selected DCIS patients (Intra et al. 2003, 2008; Moran et al. 2007; Sakorafas et al. 2008).

The rate of positive SLN ranged from 10% to 30% in patients with DCISM. So these patients should undergo SLNB. In addition, if the patients have DCIS of sufficient extent on mammography or MRI that a mastectomy will be advised then simultaneous SLNB should also be performed. Moreover, if the final histologic examination indicates an invasive or microinvasive focus, SLNB should be recommended as a second step (Takács et al. 2009).

In some instances, metastases could be found in pure DCIS (range from 0% to 13%). It is due to the underdiagnosis of DCIS for which the pathology sections simply missed the invasive area. In that case, it is not "true" pure DCIS. Another possibility is that iatrogenic displacement and physiologically drains into SLN during the healing process. Lots of factors, including benign transport and iatrogenic displacement, could create the situation whereby an initial needling procedure can cause epithelial cells to be displaced into a healing biopsy site from which they are physiologically transported to SLN. The potential for such cells to be overinterpreted as evidence of metastatic carcinoma is very real (Bleiweiss et al. 2005). In addition, the risk of additional metastases in patients with isolated tumor cells in SLN is very low. Moore et al. showed that the likelihood of finding isolated tumor cells in the SLN was related to the invasiveness of biopsy rather than the aggressiveness of the tumor (Moore et al. 2004). No adjuvant treatment is indicated in this group now.

The prognostic significance of SLN micrometastases is far from being understood. Although some studies have found no association between SLN micrometastases and prognosis, others have shown strong support for the prognostic power of SLN micrometastases. Reed et al. (2009) found a significantly shorter disease-free survival for 82 patients with retrospectively found SLN micrometastases out of 1259 patients enrolled in an adjuvant therapy trial. Cox et al. (2008) confirmed similar findings. In addition, Susnik et al. (2004) indicated that the presence of SLN micrometastases was significantly associated with the development of distant metastases in low-risk patients. So we recommend that further treatment is indicated in DCIS patients with SLN micrometastases.

Conclusions

Despite the widespread use of SLNB in breast cancer patients, controversies remain in DCIS. DCIS is associated with increased risk of invasive breast cancer. The potential benefit of accurately upstaging patients with DCIS and the minimal invasiveness of SLNB justify use of SLNB in selected high-risk DCIS patients. At lease patients with DCISM, have DCIS of sufficient extent on mammography or MRI, or indicated invasive or microinvasive focus by final histologic examination, are recommended for SLNB. Moreover, large randomized trials to evaluate the usefulness of SLNB in DCIS patients after long-term follow-up on local control and survival are required for further evaluation.

Acknowledgments

We thank Dr. Yonghui Liao, Dr. Fujisawa Noriyoshi and Dr. vikram Raut for their critical comments and advice. This work was supported by Chinese Government Scholarship no. 2009659015.

Conflict of Interest

All authors have no conflict of interest.

References

Ansari, B., Ogston, S.A., Purdie, C.A., Adamson, D.J., Brown, D.C. & Thompson, A.M. (2008) Meta-analysis of sentinel node biopsy in ductal carcinoma in situ of the breast. *Br. J. Surg.*, **95**, 547-554.

Berveiller, P., Mir, O., Veyrie, N. & Barranger, E. (2010) The sentinel-node concept: a dramatic improvement in breast-cancer surgery. *Lancet Oncol.*, **11**, 906.

Bianchi, S. & Vezzosi, V. (2008) Microinvasive carcinoma of the breast. *Pathol. Oncol. Res.*, **14**, 105-111.

Bleiweiss, I.J., Nagi, C.S. & Jaffer, S. (2005) Axillary sentinel lymph nodes can be falsely positive due to iatrogenic displacement and transport of benign epithelial cells in patients with breast carcinoma. *J. Clin. Oncol.*, **24**, 2013-2018.

Collado, M.V., Ruiz-Tovar, J., García-Villanueva, A., Rojo, R., Latorre, L., Rioja, M.E. & González-Palacios, F. (2010) Sentinel lymph node biopsy in selected cases of ductal carcinoma in situ. *Clin. Transl. Oncol.*, **12**, 499-502.

Cox, C.E., Kiluk, J.V., Riker, A.I., Cox, J.M., Allred, N., Ramos, D.C., Dupont, E.L., Vrcel, V., Diaz, N. & Boulware, D. (2008) Significance of sentinel lymph node micrometastases in human breast cancer. *J. Am. Coll. Surg.*, **206**, 261-268.

Derkx, F., Maaskant-Braat, A.J., van der Sangen, M.J., Nieuwenhuijzen, G.A., van de Poll-Franse, L.V., Roumen, R.M. & Voogd, A.C. (2010) Staging and management of axillary lymph nodes in patients with local recurrence in the breast or chest wall after a previous negative sentinel node procedure. *Eur. J. Surg. Oncol.*, **36**, 646-651.

Doyle, B., Al-Mudhaffer, M., Kennedy, M.M., O'Doherty, A., Flanagan, F., McDermott, E.W., Kerin, M.J., Hill, A.D. & Quinn, C.M. (2009) Sentinel lymph node biopsy in patients with a needle core biopsy diagnosis of ductal carcinoma in situ: is it justified? *J. Clin. Pathol.*, **62**, 534-538.

Espina, V., Mariani, B.D., Gallagher, R.I., Tran, K., Banks, S., Wiedemann, J., Huryk, H., Mueller, C., Adamo, L., Deng, J., Petricoin, E.F., Pastore, L., Zaman, S., Menezes, G., Mize, J., Johal, J., Edmiston, K. & Liotta, L.A. (2010) Malignant precursor cells pre-exist in human breast DCIS and require autophagy for survival. *PLoS One*, **5**, e10240.

Gipponi, M., Bassetti, C., Canavese, G., Catturich, A., Di Somma, C., Vecchio, C., Nicolò, G., Schenone, F., Tomei, D. & Cafiero, F. (2004) Sentinel lymph node as a new marker for therapeutic planning in breast cancer patients. *J. Surg. Oncol.*, **85**, 102-111.

Intra, M., Rotmensz, N., Veronesi, P., Colleoni, M., Iodice, S., Paganelli, G., Viale, G. & Veronesi, U. (2008) Sentinel node biopsy is not a standard procedure in ductal carcinoma in situ of the breast: the experience of the European institute of oncology on 854 patients in 10 years. *Ann. Surg.*, **247**, 315-319.

Intra, M., Veronesi, P., Mazzarol, G., Galimberti, V., Luini, A., Sacchini, V., Trifirò, G., Gentilini, O., Pruneri, G., Naninato, P., Torres, F., Paganelli, G., Viale, G. & Veronesi, U. (2003) Axillary sentinel lymph node biopsy in patients with pure ductal carcinoma in situ of the breast. *Arch. Surg.*, **138**, 309-313.

Maass, N., Alkasi, O., Bauer, M., Jonat, W., Souchon, R. & Meinhold-Heerlein, I. (2009) Actual management of ductal carcinoma in situ of the breast. *Arch. Gynecol. Obstet.*, **280**, 699-705.

Mittendorf, E.A., Arciero, C.A., Gutchell, V., Hooke, J. & Shriver, C.D. (2005) Core biopsy diagnosis of ductal carcinoma in situ: an indication for sentinel lymph node biopsy. *Curr. Surg.*, **62**, 253-257.

Moore, K.H., Sweeney, K.J., Wilson, M.E., Goldberg, J.I., Buchanan, C.L., Tan, L.K., Liberman, L., Turner, R.R., Lagios, M.D., Cody III, H.S., Giuliano, A.E., Silverstein, M.J. & Van, Zee, K.J. (2007) Outcomes for women with ductal carcinoma-in-situ and a positive sentinel node: a multi-institutional audit. *Ann. Surg. Oncol.*, **14**, 2911-2917.

Moore, K.H., Thaler, H.T., Tan, L.K., Borgen, P.I. & Cody, H.S. 3rd. (2004) Immunohistochemically detected tumor cells in the sentinel lymph nodes of patients with breast carcinoma: biologic metastasis or procedural artifact? *Cancer*, **100**, 929-934.

Moran, C.J., Kell, M.R., Flanagan, F.L., Kennedy, M., Gorey, T.F. & Kerin, M.J. (2007) Role of sentinel lymph node biopsy in high-risk ductal carcinoma in situ patients. *Am. J. Surg.*, **194**, 172-175.

Murphy, C.D., Jones, J.L., Javid, S.H., Michaelson, J.S., Nolan, M.E., Lipsitz, S.R., Specht, M.C., Lesnikoski, B.A., Hughes, K.S., Gadd, M.A. & Smith, B.L. (2008) Do sentinel node micrometastases predict recurrence risk in ductal carcinoma in situ and ductal carcinoma in situ with microinvasion? *Am. J. Surg.*, **196**, 566-568.

Polom, K., Murawa, D., Wasiewicz, J., Nowakowski, W. & Murawa, P. (2009) The role of sentinel node biopsy in ductal carcinoma in situ of the breast. *Eur. J. Surg. Oncol.*, **35**, 43-47.

Reed, J., Rosman, M., Verbanac, K.M., Mannie, A., Cheng, Z. & Tafra, L. (2009) Prognostic implications of isolated tumor cells and micrometastases in sentinel nodes of patients with invasive breast cancer: 10-year analysis of patients enrolled in the prospective East Carolina University/Anne Arundel Medical Center Sentinel Node Multicenter Study. *J. Am. Coll. Surg.*, **208**, 333-340.

Sakorafas, G.H., Farley, D.R. & Peros, G. (2008) Recent advances and current controversies in the management of DCIS of the breast. *Cancer,* Treat. Rev., **34**, 483-497.

Sakr, R., Barranger, E., Antoine, M., Prugnolle, H., Daraï, E. & Uzan, S. (2006) Ductal carcinoma in situ: value of sentinel lymph node biopsy. *J. Surg. Oncol.*, **94**, 426-430.

Sakr, R., Bezu, C., Raoust, I., Antoine, M., Ettore, F., Darcourt, J., Kerrou, K., Daraï, E., Rouzier, R. & Uzan, S. (2008) Value of sentinel lymph node biopsy in breast ductal carcinoma in situ upstaged to invasive carcinoma. *Breast J.*, **14**, 55-60.

Susnik, B., Frkovic-Grazio, S. & Bracko, M. (2004) Occult micrometastases in axillary lymph nodes predict subsequent distant metastases in stage I breast cancer: a case-control study with 15-year follow-up. *Ann. Surg. Oncol.*, **11**, 568-572.

Tada, K., Ogiya, A., Kimura, K., Morizono, H., Iijima, K., Miyagi, Y., Nishimura, S., Makita, M., Horii, R., Akiyama, F. & Iwase, T. (2010) Ductal carcinoma in situ and sentinel lymph node metastasis in breast cancer. *World. J. Surg. Oncol.*, **8**, 6.

Takács, T., Paszt, A., Szentpáli, K., Ormándi, K., Lázár, M., Pálka, I., Kahán, Z. & Lázár, G. (2009) Importance of sentinel lymph node biopsy in surgical therapy of in situ breast cancer. *Pathol. Oncol. Res.*, **15**, 329-333.

Veronesi, U., Galimberti, V., Mariani, L., Gatti, G., Paganelli, G., Viale, G., Zurrida, S., Veronesi, P., Intra, M., Gennari, R., Rita, Vento, A., Luini, A., Tullii, M., Bassani, G. & Rotmensz, N. (2005) Sentinel node biopsy in breast cancer: early results in 953 patients with negative sentinel node biopsy and no axillary dissection. *Eur. J. Cancer.*, **41**, 231-237.

van la Parra, R.F., Ernst, M.F., Barneveld, P.C., Broekman, J.M., Rutten, M.J. & Bosscha, K. (2008) The value of sentinel lymph node biopsy in ductal carcinoma in situ (DCIS) and DCIS with microinvasion of the breast. *Eur. J. Surg. Oncol.*, **34**, 631-635.

Virnig, B.A., Tuttle, T.M., Shamliyan, T. & Kane, R.L. (2010) Ductal carcinoma in situ of the breast: a systematic review of incidence, treatment, and outcomes. *J. Natl. Cancer Inst.*, **102**, 170-178.

Wilkie, C., White, L., Dupont, E., Cantor, A. & Cox, C.E. (2005) An update of sentinel lymph node mapping in patients with ductal carcinoma in situ. *Am. J. Surg.*, **190**, 563-566.

Yeung, H.W., Cody III, H.S., Turlakow, A., Riedel, E.R., Fey, J., Gonen, M., Nuñez, R., Yeh, S.D. & Larson, S.M. (2001) Lymphoscintigraphy and sentinel node localization in breast cancer patients: a comparison between 1-day and 2-day protocols. *J. Nucl. Med.*, **42**, 420-423.

Yi, M., Krishnamurthy, S., Kuerer, H.M., Meric-Bernstam, F., Bedrosian, I., Ross, M.I., Ames, F.C., Lucci, A., Hwang, R.F. & Hunt, K.K. (2008) Role of primary tumor characteristics in predicting positive sentinel lymph nodes in patients with ductal carcinoma in situ or microinvasive breast cancer. *Am. J. Surg.*, **196**, 81-87.

Model-Based Reconstruction Integrated With Fluence Compensation for Photoacoustic Tomography

Shuhui Bu, *Member, IEEE*, Zhenbao Liu*, *Member, IEEE*, Tsuyoshi Shiina, *Member, IEEE*, Kengo Kondo, Makoto Yamakawa, *Member, IEEE*, Kazuhiko Fukutani, Yasuhiro Someda, and Yasufumi Asao

***Abstract*—Photoacoustic (PA) tomography (PAT) is a rapidly developing imaging modality that can provide high contrast and spatial-resolution images of light-absorption distribution in tissue. However, reconstruction of the absorption distribution is affected by nonuniform light fluence. This paper introduces a reconstruction method for reducing amplification of noise and artifacts in low-fluence regions. In this method, fluence compensation is integrated into model-based reconstruction, and the absorption distribution is iteratively updated. At each iteration, we calculate the residual between detected PA signals and the signals computed by a forward model using the initial pressure, which is the product of estimated voxel value and light fluence. By minimizing the residual, the reconstructed values converge to the true absorption distribution. In addition, we developed a matrix compression method for reducing memory requirements and accelerating reconstruction speed. The results of simulation and phantom experiments indicate that the proposed method provides a better contrast-to-noise ratio (CNR) in low-fluence regions. We expect that the capability of increasing imaging depth will broaden the clinical applications of PAT.**

***Index Terms*—Fluence compensation, model-based reconstruction, photoacoustic (PA).**

I. Introduction

THE photoacoustic (PA) effect [1]–[3] means the generation of acoustic waves by the absorption of electromagnetic (EM) energy. In photoacoustic tomography (PAT), by illuminating a target with a short pulse laser, stress waves are produced due to the thermoelastic expansion. Acoustic sensors are placed at surrounding positions to detect PA signals, and then the absorption source is recovered from the detected PA signals through a reconstruction algorithm. PAT combines the advantages of optical and acoustical methods: sensitive optical absorption contrast and low acoustic scattering in soft tissue. Because light energy is converted to ultrasound that has much less absorption and scattering than light, PAT has much better spatial resolution than traditional optical modalities at depths exceeding the optical ballistic regime. The hemoglobin molecule in blood is a primary absorber in tissue; hence, the absorbed optical-energy distribution reconstructed by PAT can provide the local structure of blood circulation. In the early stage of cancer, capillary vessel density increases. Thus, PAT could detect cancer, especially the breast cancer.

Reconstruction algorithms for PAT have been extensively studied in recent decades [1], [2]. The simplest reconstruction method is delay and sum [4], which is a basic beam-forming technique used in ultrasound imaging. Further improvement can be achieved by utilizing the coherence factor [5] and the minimum variance method [6]. A filtered back-projection (FBP) method [7], [8] is based on inverse Radon transformation [9] and assumes that an object is located near the center of scanning area and far away from detectors. These methods have the advantage of convenient and fast calculation. When the projection data are collected in full view, the FBP algorithm can reconstruct good-quality images with a high signal-to-noise ratio (SNR). However, if the collected data are not in full view, artifacts appear in the reconstructed images. Besides the approximation methods, analytic reconstruction methods with fewer assumptions are proposed to obtain exact reconstruction, for example, universal back-projection (UBP) methods [10], [11] and Fourier domain reconstruction methods [12]–[14]. These analytic reconstruction methods also require enclosed detection for circular scanning or an unbounded open surface for planar scanning, which are generally difficult to implement in a clinical situation. To overcome the limited-view problem, model-based reconstruction methods [15]–[23] (also called iterative reconstruction methods) have been investigated. In these methods, the inverse problem is converted into solving an optimization problem by minimizing the error between detected PA signals and calculated signals from a forward model. In general, although this type of methods needs more computation, it needs fewer detecting sensors and, thus, less acquisition time. It is also able to model nonideal physical conditions and measurement environments. Therefore, the degradation of reconstructed images caused by acoustic inhomogeneity and attenuation can be resolved.

One major problem with PAT reconstruction is that the reconstructed information is affected by nonuniform light fluence,

Manuscript received May 18, 2011; revised September 7, 2011 and December 26, 2011; accepted February 4, 2012. Date of publication February 13, 2012; date of current version April 20, 2012. This work was supported in part by the Innovative Techno-Hub for Integrated Medical Bio-Imaging Project of the Special Coordination Funds, from the Ministry of Education, Culture, Sports, Science, and Technology (MEXT), Japan, and in part by the Natural Science Foundation of China (NSFC) (61003137) and the Scientific Research Foundation (SRF) for Returned Overseas Chinese Scholars (ROCS) and Northwestern Polytechnical University (NWPU) fundamental fund. *Asterisk indicates corresponding author.*

S. Bu is with the Northwestern Polytechnical University, Xian 710072, China, and also with the Kyoto University, Kyoto 606-8501, Japan (e-mail: bushuhui@nwpu.edu.cn).

*Z. Liu is with the Northwestern Polytechnical University, Xian 710072, China (e-mail: liuzhenbao@nwpu.edu.cn).

T. Shiina, K. Kondo, and M. Yamakawa are with Kyoto University, Kyoto 606-8501, Japan (e-mail: shiina@hs.med.kyoto-u.ac.jp; k-kondo@hs.med.kyoto-u.ac.jp; m.yamakawa@kt8.ecs.kyoto-u.ac.jp).

K. Fukutani, Y. Someda, and Y. Asao are with the Medical Imaging Project, Canon Inc., Tokyo 146-8501, Japan (e-mail: fukutani.kazuhiko@canon.co.jp; someda.yasuhiro@canon.co.jp; asao.yasufumi@canon.co.jp).

Color versions of one or more of the figures in this paper are available online at http://ieeexplore.ieee.org.

Digital Object Identifier 10.1109/TBME.2012.2187649

because tissue absorbs and scatters light so that light fluence decreases along the direction of light penetration. The pixels or voxels in reconstructed PAT images are used to represent the level of absorbed optical energy, which is the product of absorption coefficient and light fluence. Therefore, the contrast-to-noise ratio (CNR) in a low-fluence region of a reconstructed image is low. Cox *et al.* [24] proposed a simple iterative method for quantitative reconstruction, where the fluence compensation is performed after image reconstruction. Since the CNR in low-fluence regions in the reconstructed images is low, amplification of the image pixels also amplifies noise and artifacts, which leads to decrease in the image quality. Yuan *et al.* [25] proposed a quantitative reconstruction method using a diffusion equation based on the regularized Newton method. However, the PAT images need segmenting in order to obtain prior structural information. Cox *et al.* [26] extended their work [24] so that chromophore distributions can be estimated by using multi-wavelength excitation and gradient-based optimization. Rosenthal *et al.* [27], [28] proposed a sparse representation method for quantitative reconstruction based on the different spatial distribution properties of light fluence and absorption. Although this method does not require the parameter-based fluence distribution, errors occur under nonuniform boundary illumination. Zemp [29] proposed a method for quantitative reconstruction using multiple optical sources even when the Grüneisen coefficient varies spatially, while the reconstruction and transducer bandwidth in this method must be ideal. Their recent research [30] relaxed the limitation of an ideal transducer bandwidth to a more general case.

Because the light fluence, absorption, and scattering coefficient distribution, and even the Grüneisen coefficient are unknown, quantitative reconstruction is highly underdetermined. Therefore, it is very difficult to reconstruct an accurate absorption distribution. In this study, we focus on fluence compensation in order to achieve much clearer reconstruction in low-fluence regions by assuming that the Grüneisen coefficient is constant in the region of interest (ROI) and that the background absorption and scattering distribution are approximately known. Although the reconstructed absorption value is not accurate, the improved imaging depth will greatly facilitate clinical diagnosis. Our proposed method integrates fluence compensation into model-based reconstruction in order to avoid degrading image quality in low-fluence regions due to amplification of noise and artifacts. In contrast with conventional model-based reconstruction methods [15]–[17], the image reconstructed by this method is the absorption distribution. Because feedback is performed at each iteration, the amplification of noise and artifacts can be minimized. The advantages of the proposed method are that reconstruction can be performed under arbitrary illumination conditions, fewer assumptions are required, and noise and artifacts in low-fluence regions of the reconstructed images are reduced. In addition, this method can inherit the merits of the model-based reconstruction method, such as fewer limited-view artifacts [15], fewer artifacts due to nonuniform sound speed [18], and less degradation in lateral resolution [22], [23]. The results of simulation and phantom experiments indicate that the proposed method performs better than conventional methods.

Our proposed method belongs to model-based reconstruction, and such reconstruction requires a large amount of memory and a long calculation time. In order to overcome these limitations, we developed matrix compression methods. By utilizing these methods, the matrix can be compressed to 1/250 its size; hence, our proposed reconstruction method can be implemented with a conventional computer at a high speed.

The rest of this paper is organized as follows. Section II presents the principle of the proposed method. The numerical simulation and phantom experiments are described in Section III. We discuss our overall findings in Section IV. Finally, we conclude our study in Section V.

II. Method

A. Theory of Fluence Compensation and Reconstruction

A PA wave generated in an acoustically homogenous and nonviscous medium can be described as [31], [32]

$$\nabla^2 p(\mathbf{r},t) - \frac{1}{v_s^2}\frac{\partial^2}{\partial t^2}p(\mathbf{r},t) = -\frac{\beta}{C_p}\frac{\partial}{\partial t}H(\mathbf{r},t) \tag{1}$$

where $H(\mathbf{r},t)$ is a heating function defined as the thermal energy converted at position $\mathbf{r}$ and time t by EM radiation per unit volume per unit time, C_p is the isobaric specific heat, β is the coefficient of isobaric volume expansion, and v_s is acoustic speed.

The amount of heat generated in tissue is generally proportional to the input light intensity and the absorption coefficient

$$H(\mathbf{r},t) = \mu_a(\mathbf{r})\Phi(\mathbf{r},t). \tag{2}$$

Here, μ_a is the absorption coefficient, and Φ is the optical fluence. Under the conditions of both thermal and stress confinement, the heating time can be treated as a delta function, such as $H(\mathbf{r},t) \approx \mu_a(\mathbf{r})\Phi(\mathbf{r})\delta(t)$. The initial pressure p_0 of the absorber at position $\mathbf{r}$ can be calculated by

$$\begin{aligned} p_0(\mathbf{r}) &= \frac{v_s^2\beta}{C_p}\mu_a(\mathbf{r})\Phi(\mathbf{r}) \\ &= \Gamma\mu_a(\mathbf{r})\Phi(\mathbf{r}) \end{aligned} \tag{3}$$

where Γ is the Grüneisen coefficient expressed as $\Gamma = \beta v_s^2/C_p$. Here, we assume that the Grüneisen coefficient is constant in the imaging ROI.

Wave equation (1) can be solved by using a Green function approach [1]. Under acoustic stress confinement, the heating process is treated approximately as a Dirac delta function, and the solution is

$$p(\mathbf{r},t) = \frac{\beta}{4\pi C_p}\frac{\partial}{\partial t}\int_V d\mathbf{r}'\frac{\mu_a(\mathbf{r}')\Phi(\mathbf{r}')}{|\mathbf{r}-\mathbf{r}'|}\delta\left(t - \frac{|\mathbf{r}-\mathbf{r}'|}{v_s}\right). \tag{4}$$

The aforementioned equation describes a relationship in which the detected PA pressure at position $\mathbf{r}$ and time t comes from sources over a spherical surface centered at $\mathbf{r}$ with a radius of $|\mathbf{r}-\mathbf{r}'|$. For an inverse problem to (4), a reconstruction equation is derived for exact reconstruction of initial pressure distribution in an analytic reconstruction method such as UBP [10]. The only way to obtain the absorption distribution is to compensate light

fluence after the reconstruction of initial pressure distribution. This process also amplifies noise and artifacts, especially under limited-view conditions, resulting in a low-quality image.

In the proposed method, we separate the light fluence and the absorption coefficient at each voxel position. The absorption coefficients are estimated by a model-based method. We assume mean absorption and scattering coefficients for the background material. In this case, the light fluence distribution can be accurately obtained by a Monte Carlo method [33] after capturing incident light patterns. Another common approach for computing light fluence is to solve a photon diffusion equation using the finite element method [34], [35] at a high speed. However, the Monte Carlo solution can be greatly speed up using a high-performance parallel implementation.

Based on the (4), the forward model for calculating PA signals can be expressed in a matrix form as

$$\mathbf{p} = \mathbf{A}\Phi\boldsymbol{\mu}_a \tag{5}$$

where $\mathbf{A}$ denotes the system matrix representing the geometric relationship between the initial pressure and the detected PA signals, Φ is a diagonal matrix representing the light fluence, and $\mathbf{p}$ denotes the detected PA signals. The detailed form of $\mathbf{A}$ is

$$A_{i,j} = \frac{A'_{i,j+1} - A'_{i,j-1}}{2\Delta t} \tag{6}$$

where i is the index of sensor's position, j is the index of PA signal, Δt is the time interval between two sampling points, and $A'_{i,j}$ denotes the velocity potential. In the planar-measurement environment, the time of sound propagation through a voxel is longer than the sampling interval, and consequently the pressure data are not continuous after a finite-difference calculation. This process induces fluctuations with large amplitude, which prevent high-accuracy forward modeling. In this research, we assume voxel as sphere. The PA wave emitted from a small spherical source has a velocity potential profile of a Gaussian function [15], [36], [37] under the following assumption: the density distribution of absorbed energy in a sphere is a Gaussian distribution. The aforementioned assumption may lead to a problem that the accuracy of Gaussian interpolation is not very high. However, the advantage of Gaussian interpolation is that it can provide high-performance calculation. The imaging domain in this research is 3-D and large; hence, the system-matrix computation is time consuming. In order to achieve a good balance between calculation time and accuracy, the Gaussian kernel is chosen to interpolate the velocity potential data. The definition of the interpolated velocity potential item is

$$\begin{aligned} A'_{i,j} &= \frac{\beta}{4\pi C_p}\frac{h_{i,j}}{R_{i,j}} \\ R_{i,j} &= |\mathbf{r}_i - \mathbf{r}_j| \\ h_{i,j} &= \begin{cases} \exp\left(\frac{-2(R_{i,j}-t_j v_s)^2}{\Delta^2}\right) : \text{if} |t_j - \frac{R_{i,j}}{v_s}| < \Delta/v_s \\ 0 : \text{else} \end{cases} \end{aligned} \tag{7}$$

where Δ is the distance between the central points of adjacent voxels.

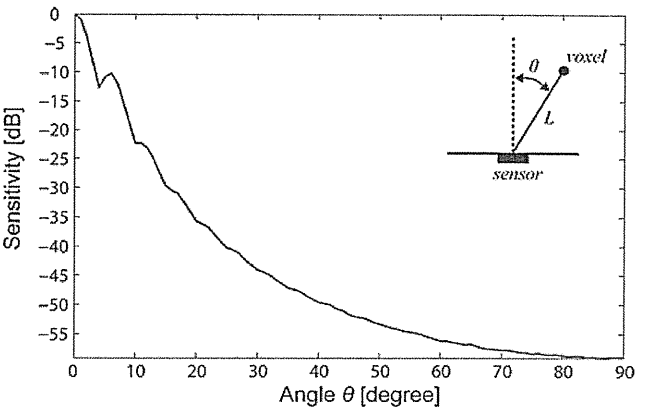

Fig. 1. Angular sensitivity of a 2×2 mm^2 unfocused rectangular transducer. The distance between transducer and target is $L = 10$ mm. The horizontal axis represents the wave incident angle θ (in degree), and the vertical axis represents the sensitivity of the transducer. The DREAM toolbox [38] was used to calculate the result.

The quantitative absorption distribution is estimated by minimizing the l_2 norm between the detected signals and the PA signals calculated by the forward model:

$$\boldsymbol{\mu}'_a = \arg\min_{\boldsymbol{\mu}_a} \|\mathbf{p}_d - \mathbf{A}\Phi\boldsymbol{\mu}_a\|_2. \tag{8}$$

Here, $\mathbf{p}_d$ represents the detected PA signals, and $\boldsymbol{\mu}'_a$ is the optimal estimation of the absorption coefficient distribution. The conjugate gradient (CG) method is used to find the optimal estimation.

B. Matrix Compression

Although model-based reconstruction for PAT has many advantages, it has a critical limitation that the system matrix consumes huge amounts of memory without matrix compression. In order to apply the proposed method to clinical situations, we developed matrix-compression methods to reduce the memory requirement. First, matrix $\mathbf{A}$ is a sparse matrix in which more than 99% of the entries are zero. The required memory can be greatly reduced by using the compressed sparse row (CSR) format [40], where nonzero entries are stored in continuous memory locations and corresponding column indices are stored in an integer array. We use another integer array to store the index of first nonzero entry in each row.

In PAT, the ultrasound transducer is generally assumed to detect pressure waves in directions from 0° to 90° with the same sensitivity; however, in real situations the sensitivity is not uniform due to the finite-sized unfocused transducer. The spatial impulse response (SIR) of the transducer introduces limited detection angles, waveform distortion, and time-delay errors for reconstruction [22], [23]. For example, the angular sensitivity of a 2×2 mm^2 unfocused rectangular transducer is plotted in Fig. 1. When the incident angle is 45°, the sensitivity is −50 dB, which is less than the detectable signal level for a conventional sensor. Hence, the incident wave can be ignored. In order to compress the matrix $\mathbf{A}$, if the incident angle exceeds a given threshold, its value is set to zero so that the entry is not stored.

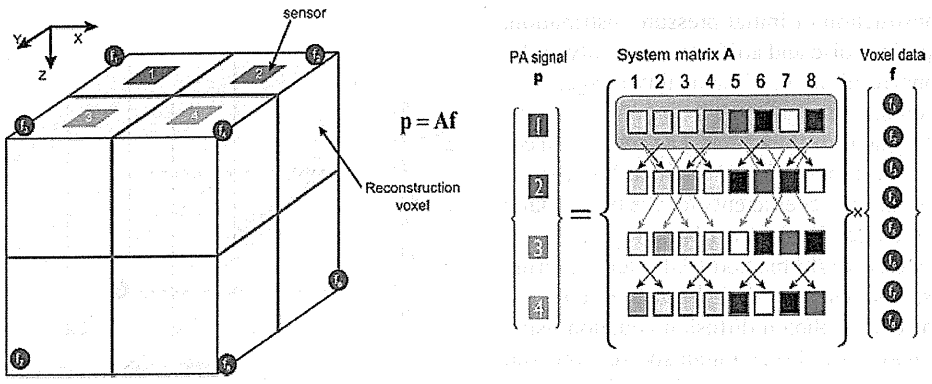

Fig. 2. Matrix compression using the symmetry of wave propagation. For simplicity, in this figure only four sensors and eight voxels are illustrated. Only the first 1/4 row of **A** is stored; coefficients in other rows can be obtained by rearranging the order of the first 1/4 row's coefficients.

With this approach, matrix **A** can be further decreased to about half its original size when the threshold value is 45°.

The matrix can be further compressed to one-fourth its original size based on the symmetry of wave propagation [21], as illustrated in Fig. 2. This figure depicts only four sensors and eight voxels. The PA signals detected by sensor 1 are calculated from the inner product $\mathbf{A}(\mathbf{1},:)\cdot\mathbf{f}$. Because sensors 2 and 1 are symmetrical about the Y-axis, the second row of **A** can be obtained by changing the X-axis order of the first row. Similarly, the third row of **A** can be obtained by changing the Y-axis order of the first row, and the fourth row of **A** can be obtained by changing the X- and Y-axis orders of the first row. Therefore, only one-fourth of the rows of **A** are necessary for reconstruction, and other rows' data can be obtained during the multiplication of sparse matrix and vector. In total, the required memory can be reduced to approximately 1/250 its original size by using the aforementioned methods.

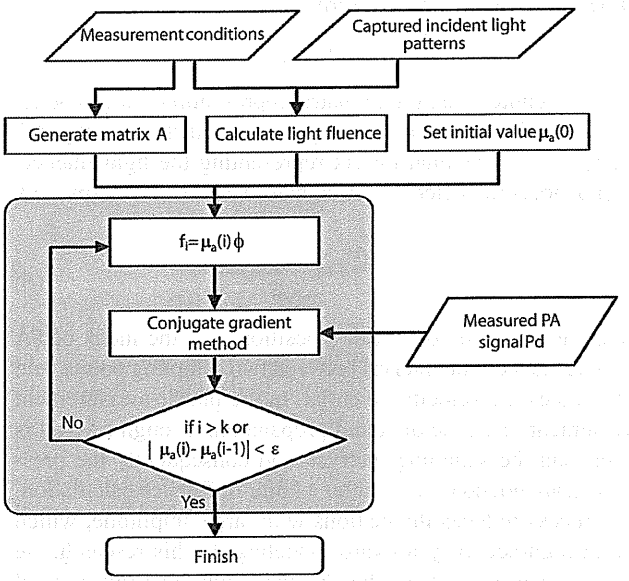

Fig. 3. Flow-chart of the proposed method.

C. Implementation

The flow-chart of the proposed method is presented in Fig. 3. After the measurement conditions are determined, the system matrix **A** is calculated according to the geometry parameters. The incident light patterns are captured by a camera, and the distribution of light fluence is then calculated using the Monte Carlo method, where the previously estimated mean absorption and reduced scattering coefficients for the background material are used. The initial values of $\mu_a(i)$ are set to zeros or UBP reconstructed values. Next, the reconstruction is performed, and the CG method is adopted to solve the optimization problem. In each CG iteration, the residual is computed by using the precalculated absorbed energy $\mathbf{f}_i$, while the value is updated to the $\mu_a(i)$. This differs slightly from the traditional CG method, because using the updated absorption coefficients to calculate the residual at each iteration leads to divergence, which prevents convergence to the true value. In our experiments, the optimal number of iterations in the inner CG is 5 to 8. At the outer iteration, computation is terminated when the iteration loop number exceeds a given number or the change of absorption coefficients is less than a threshold.

III. Simulation and Phantom Experiments

A. Numerical Simulation

The proposed method was evaluated by numerically simulating a hypothetical model, as illustrated in Fig. 4. In this model, five wire targets with a diameter of 0.5 mm embedded in a uniform block ($32 \times 32 \times 32$ mm^3) were simulated as shown in Fig. 4(a). The simulation parameters are summarized in Table I. The background's absorption coefficient was $\mu_a = 0.078$ cm^{-1}, and its reduced scattering coefficient was $\mu_s' = 9.306$ cm^{-1}. The absorption coefficient of the wire target was $\mu_a = 4.3$ cm^{-1}. Forward illumination (toward the probe) was used as illustrated by Fig. 4(a), and the incident light pattern is shown in Fig. 4(b), which adopts data captured by a camera as well as phantom experiment.

The light fluence was calculated by the Monte Carlo method using the incident light pattern and the mean absorption and scattering coefficients of the background. Fig. 4(c) shows the 3-D distribution of light fluence (left), light fluence distribution

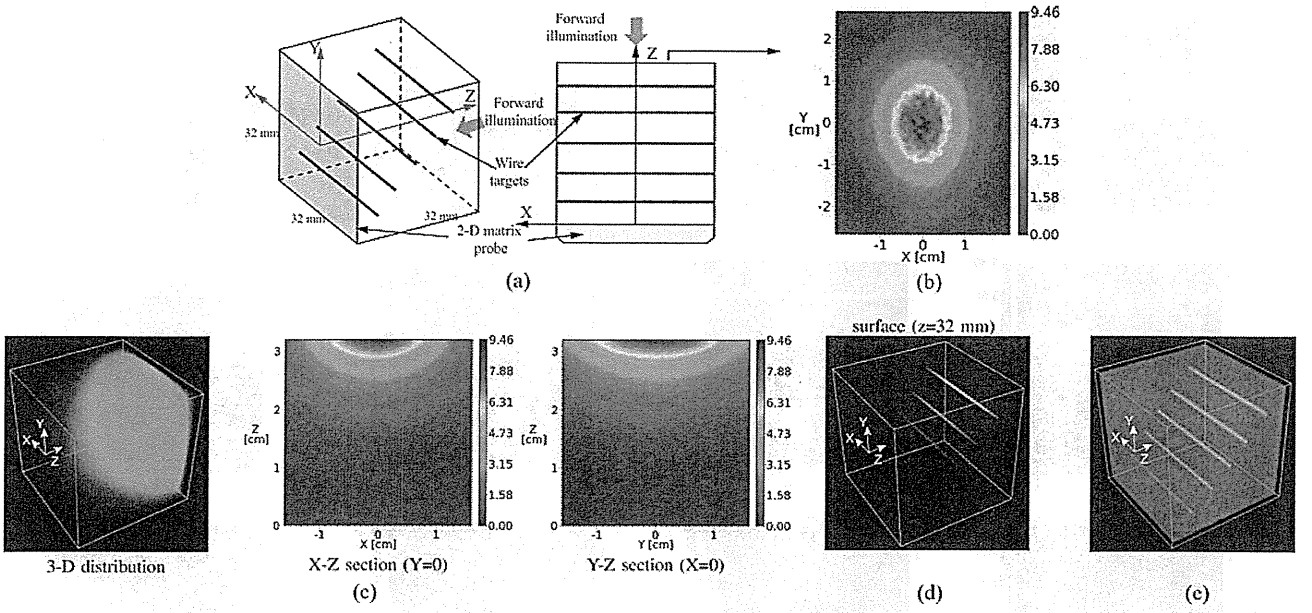

Fig. 4. Numerical simulation model. (a) Alignment of wire targets as optical absorber, ultrasound probe, and optical source. (b) Incident light pattern on the surface ($z = 32$ mm) by forward illumination. (c) Light fluence distribution calculated by the Monte Carlo method; 3-D distribution (Left), cross section of X–Z plane at $Y = 0$ (middle), Y–Z plane at $X = 0$ (right). (d) Initial pressure distribution. (e) Absorption distribution reconstructed by the proposed method.

TABLE I
SIMULATION PARAMETERS

Parameter name	Value
Sound speed	1500 m/s
Sampling frequency	20 MHz
Sampling point number	750
Sensor number in x and y axes	16
Sensor pitch in x and y axes	2.0 mm
Voxel number in x, y, and z axes	64
Voxel size in x, y, and z axes	0.5 mm

on the cross section of X–Z plane at $y = 0$ (middle), and Y–Z plane at $x = 0$ (right). The PA waves were simulated using (4), and −30-dB white noise was added. Fig. 4(d) shows the 3-D distribution of initial pressure. Finally, the 3-D absorption distribution reconstructed by the proposed method is shown in Fig. 4(e).

All programs were implemented in parallel and run on a cluster system containing six workstations. Each workstation had two quad-core Xeon 2.4-GHz CPUs. The floating point operation per second (FLOPS) of the cluster system was 251 G. It took 42 s to calculate the light fluence distribution. After the simulated PA signals were obtained, the reconstruction program was used to reconstruct the absorption distribution. The required memory of matrix $\mathbf{A}$ before compression was 402.653 GB; after compression it was reduced to 1.255 GB. The calculation time for one iteration was 0.6 s, and there were 400 iterations in total.

Fig. 5 presents the maximum intensity projection (MIP) images reconstructed by the proposed method, compared with the conventional quantitative reconstruction method, that is, UBP with fluence compensation after reconstruction. Here, MIP X–Y (top images) is the projection along the Z-axis, MIP X–Z (middle images) is the projection along the Y-axis, and MIP Z–Y (bottom image) is the projection along the X-axis.

Fig. 5(a) presents MIP images of the given absorption distribution. Fig. 5(b) presents MIP images of the absorbed optical energy distribution. The resulting MIP images in Fig. 5(c) show the absorption distribution reconstructed by the conventional method. The images reconstructed by the proposed method are presented in Fig. 5(d). The profiles along the Z-direction at $x = 0$ in MIP X–Z are presented in Fig. 5(e). The unit of absorbed optical energy images is mJ/cm^3, and the unit of absorption coefficient is cm^{-1}.

In the conventional method, the initial pressure is first reconstructed by the UBP method, and then the absorption coefficient is obtained by dividing the light fluence. The light fluence decreases rapidly in tissue, and hence the light fluence is low at the deep location. In the simulation, −30-dB white noise was added into the PA signals, and consequently noise and artifacts were produced in the UBP reconstruction. The noise and artifacts are amplified in low fluence regions after conventional fluence compensation. In contrast, these are greatly reduced by the proposed method. From the profiles, we can see that the CNR of the target at $z = 16$ mm is 6.46 for the proposed method and 1.39 for the conventional method. The CNR improvement is 4.63 times.

B. Phantom Experiment

Performances were also evaluated by a tissue-mimicking phantom with embedded absorbers as illustrated in Fig. 6(a). The base of the tissue-mimicking phantom with a size of 70 (X) × 120 (Y) × 50 (Z) mm^3 was made with urethane gel and curing agent. The speed of sound in the base phantom was 1391 m/s. Rubber wires with 0.3 mm diameter were embedded in the base phantom. The absorption and reduced scattering coefficients of the base phantom were 0.078 and 9.306 cm^{-1} at a wavelength of 797 nm. We utilized a spectrophotometer to measure the

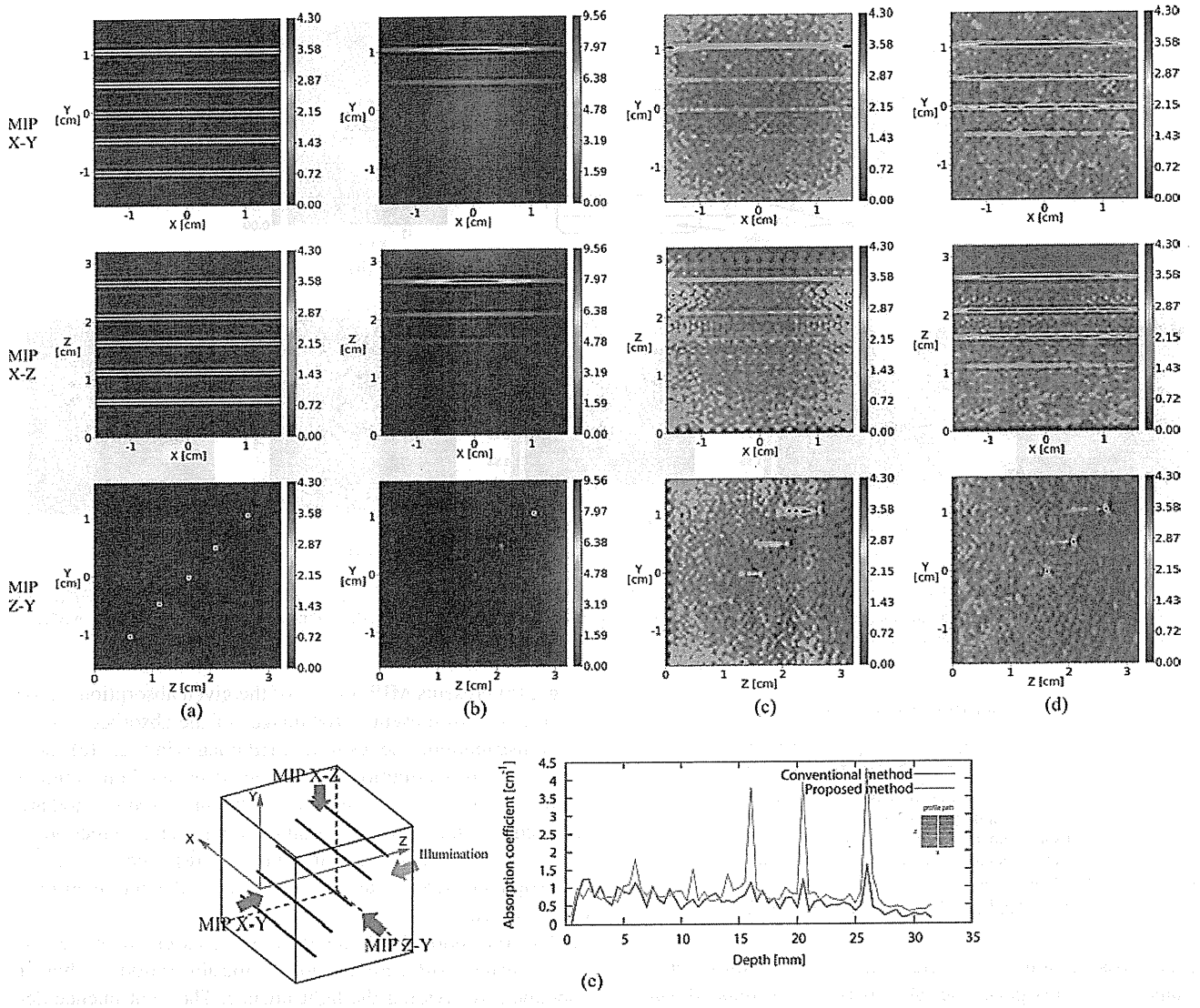

Fig. 5. Simulation model and images reconstructed by the proposed method and the conventional quantitative reconstruction method. Each depicts the MIP image. (a) Simulation model: given absorption distribution. (b) Absorbed optical energy distribution. (c) Resulting images of absorption coefficient reconstructed by the conventional quantitative reconstruction method. (d) Resulting images of absorption coefficient reconstructed by the proposed method. (e) Profiles along the Z-direction at $x = 0$ in MIP X–Z.

reflection and transmission properties of the phantom sample. An iterative method was adopted to estimate the optimal optical properties of the sample. First, initial optical parameters were selected. At each iteration, the Monte Carlo method was used to calculate the reflection and transmission values, and the Newton method was used to update the estimated optical parameters. The iteration was terminated when the differences between measured and calculated values of reflection and transmission were less than a threshold. The last estimated values were regarded as the optimal absorption and reduced scattering coefficients of the sample.

A PA imaging system with dual illumination [39] was utilized in the phantom experiment, where dual lasers illuminate the target so that it is possible to image deeper regions in tissues. Two sets of a Ti:Sa laser (LT-2211, LOTIS TII) pumped by a Q-switched Nd:YAG laser (LS-2137, LOTIS TII) were adopted as the excitation source to provide 15-ns laser pulses with a 10-Hz pulse repetition rate. One laser was used for backward illumination (probe side), and the other for the forward direction (opposite side from the probe), as illustrated in Fig. 6(a). A wavelength of 797 nm was adopted in this experiment. The maximum incident light energy densities from backward and forward illumination on the sample surface were 3.48 and 9.46 mJ/cm^2, respectively. The distributions of incident light energy density captured by a camera are given in Fig. 6(b) and (c), where the unit of the colorbar is mJ/cm^2. The light fluence was calculated by the Monte Carlo method, as shown in Fig. 6(d). The profile of light fluence at the center of the probe along the depth direction is plotted in Fig. 6(e).

A 2-D 345-element [15 (X) $\times$ 23 (Y)] matrix probe with element size of 2 $\times$ 2 mm^2 was used in our system. The rectangular shape of the matrix probe enables direct illumination of tissue

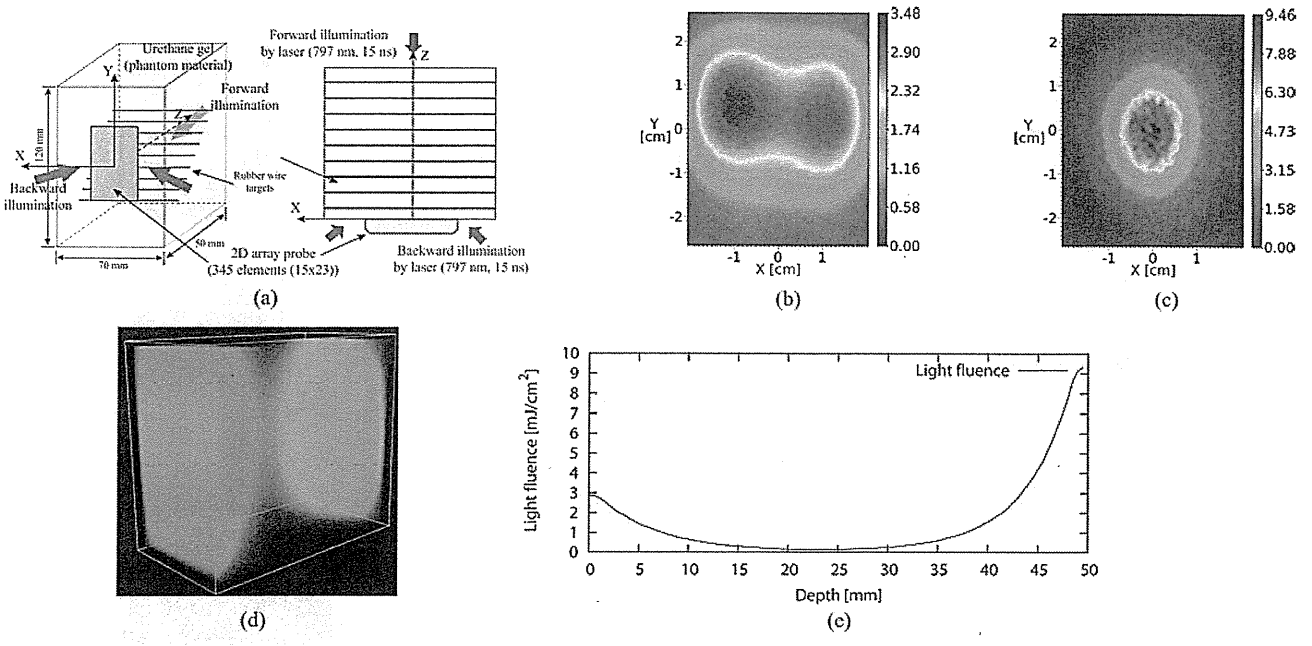

Fig. 6. Configuration of phantom experiment. (a) Phantom and settings of probe and optical source. (b) Incident light pattern (light energy density distribution) on the back side (probe side); the unit of the colorbar is mJ/cm^2. (c) Incident light pattern on the forward side (opposite side from probe); the unit of the colorbar is mJ/cm^2. (d) Light fluence calculated by the Monte Carlo method. (e) Profile of light fluence at the center of the probe along the depth direction.

surfaces in front of the array transducer through a 10-mm thick holding plate. The transducer frequency was designed to be 1 MHz with a bandwidth greater than 70%. The array had a detection area of 30×46 mm^2. Custom-made front-end electronics and a data-acquisition system were employed to obtain PA signals for image reconstruction. The front-end electronics consist of 345-channel receivers. We adopted a fixed amplifier gain of 40 dB, a sampling rate of 20 MHz, and 1280 sampling points. The received PA signals were amplified, filtered, and digitized in the data-acquisition system. The digitized PA signals were transferred to a PC for further signal processing and image reconstruction. In the reconstruction, the voxel size was set to 0.5 mm for all axes, and the reconstruction range was 28 $(X) \times 44$ $(Y) \times 50$ (Z) mm^3.

The images were reconstructed on the same cluster system as described in Section III-A. It took 65 seconds to calculate the light fluence distribution. In order to obtain the best performance, only PA signals from 14×22 channels were used, although the matrix probe has 15×23 channels. The required memory for the matrix $\mathbf{A}$ before compression was 1.554 TB; after compression, the size was reduced to 6.250 GB. The calculation time for one iteration was 1.2 seconds, and there were 240 iterations in total.

The resulting images are presented in Fig. 7. Fig. 7(a) and (b) presents MIP images reconstructed by the UBP method without and with fluence compensation, respectively. The MIP images reconstructed by the proposed method are presented in Fig. 7(c). The profiles along the Z-direction at $x = 0$ in MIP X–Z are plotted in Fig. 8.

In the resulting images, the display is in an arbitrary unit. In this research, the absolute values of absorption coefficient can be reconstructed in theory, but are actually difficult to calculate for the following reasons. 1) The attenuation of ultrasound wave is not considered, and the Grüneisen coefficients are assumed constant in the whole region. 2) In our experiment, it is difficult to measure the absorption coefficient of rubber wires. Therefore, it is difficult to normalize the reconstructed value to the absolute value. On the other hand, the main objective of our research is to image macroscopic capillary vessel density; therefore, the absolute value of absorption coefficient is not very necessary. As a result, the reconstructed images of the phantom experiment are displayed in an arbitrary unit.

The resulting images indicate that the absorption distribution reconstructed using the proposed method is better than that using the conventional fluence compensation method. The light fluence around $z = 25$ mm is low. In this case, the wire target at the position can hardly be seen in the resulting imaging reconstructed by the UBP without fluence compensation, and much noise and artifacts appear in the resulting images reconstructed by the conventional fluence compensation method. We compared the proposed method to the UBP with and without fluence compensation, and the evaluation parameters include mean and standard deviation of targets' absorption coefficients, and average CNR. The mean and standard deviation are 0.458 and 0.275 in the UBP without fluence compenation, 0.482 and 0.169 in the UBP with fluence compensation. Our method improved the two values to 0.624 and 0.145. The average CNR is 4.19 in the UBP with fluence compensation, and in the proposed method it is 4.84 with an improvement of 15.51%. However, we also found that the average CNR in the UBP without light fluence is 11.79, and either of fluence compensation methods yields lower values than it. The reason that CNR becomes low is that noise and artifacts amplification cannot be avoided during the fluence compensation. But in the proposed method, we

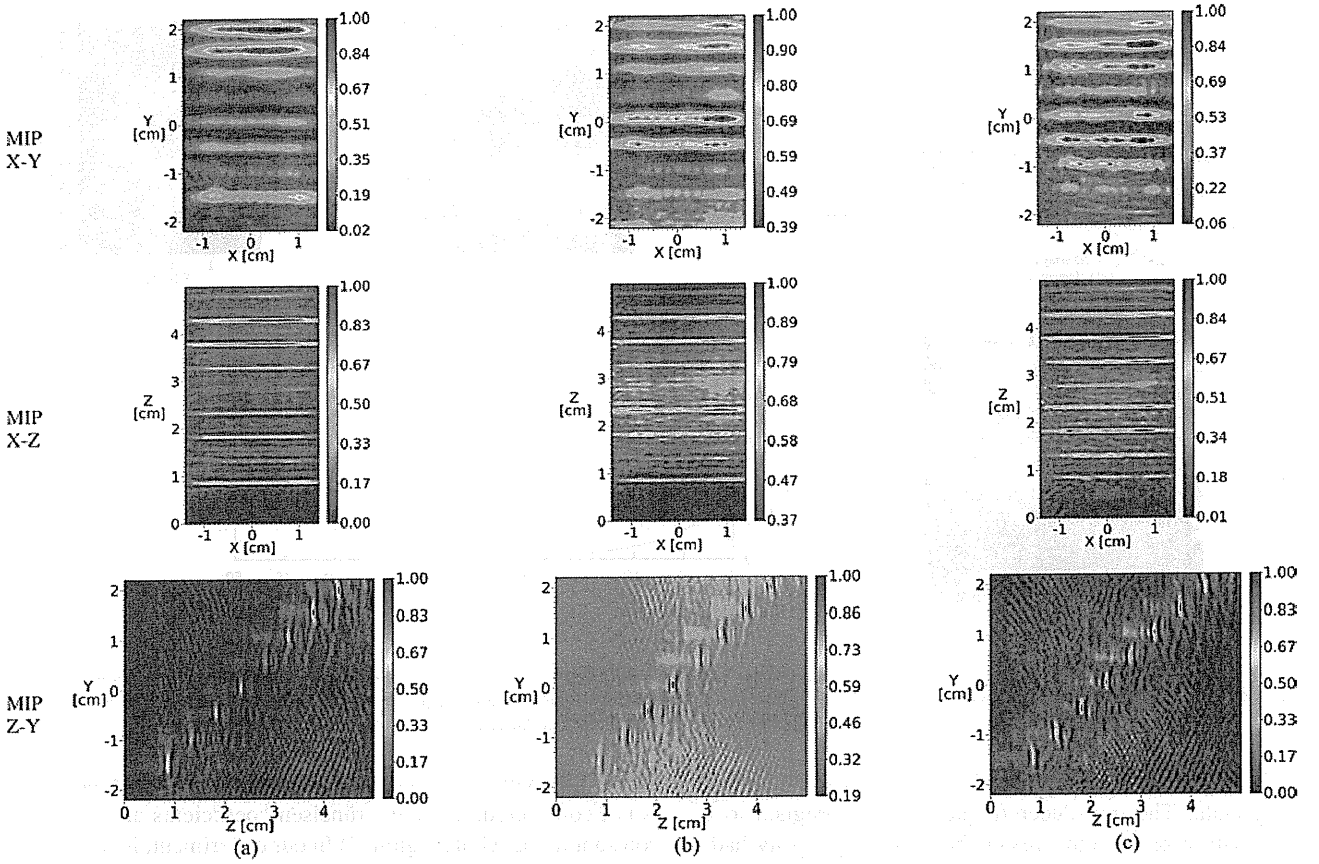

Fig. 7. Results of image reconstructed from experiment data. (a) Images reconstructed by the UBP method without fluence compensation. (b) Images reconstructed by the UBP method with conventional fluence compensation. (c) Images reconstructed by the proposed method.

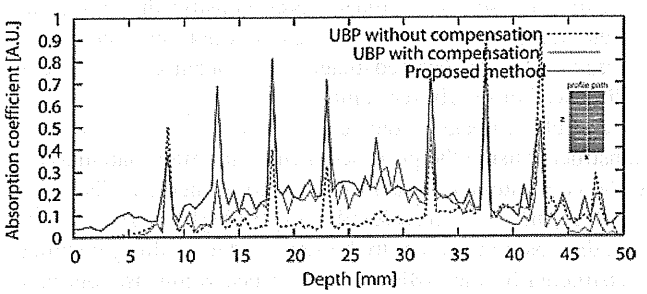

Fig. 8. Profile along Z direction at $X = 0$ in MIP X–Z.

improved the process of fluence compensation, which minimizes the overall noise and artifacts. As a result, the amplification of noise and artifacts is suppressed, and the CNR exceeds that of conventional fluence compensation method. Although the UBP without fluence compensation outperforms either of the fluence compensation methods on the CNR, the quantitative absorption coefficients are no better than them. Therefore, the proposed method achieves a better balance between CNR and quantitative reconstruction.

In addition, because the imaging region is 3-D and furthermore with a large region, which leads to extremely low values of light fluence in some local regions, the absorbed energy in these local regions is low and hence the initial pressure is low. Our system also suffers from the hardware limitations on enhancing the sensitivity of ultrasound transducer and the SNR of ADC. Based on the aforementioned two points, it becomes difficult to obtain accurate reconstruction at low fluence regions.

IV. Discussion

In this study, we assume mean absorption and reduced scattering coefficients for the background material. The light fluence distribution is calculated by the Monte Carlo method [33], using the assumed mean absorption and scattering coefficients, and captured incident light patterns. Fluence compensation and reconstruction are combined in order to achieve better performance. In the current research stage, although light fluence is calculated only once using the estimated mean absorption and reduced scattering coefficients for the background material, the proposed method has the capability to update the light fluence at each iteration using the newly estimated absorption coefficient [24]. In our method, it is important to exactly calculate the light fluence distribution for better reconstruction under the assumption of mean optical parameters are known. There exist several solutions that can overcome the restriction of optical inhomogeneity. First, a diffuse optical tomography (DOT) [41], [42] can be used to estimate the low-resolution absorption distribution so as to assist the light fluence calculation. Second, not only absorption distribution but also Grüneisen

distribution can be estimated in the multi-illumination method proposed by Zemp *et al.* [29], [30]. These methods have the potential to provide robust and accurate light fluence distribution for planar-scanning schemes.

In addition, for reducing memory requirements and accelerating reconstruction speed, we developed matrix-compression methods. The system matrix was losslessly compressed by using the CSR format and storing only one-fourth of the rows based on the symmetry of wave propagation, and further compressed with little loss based on the nonuniform angular sensitivity of ultrasound transducer. As a result, the memory required by the matrix could be effectively reduced, and the reconstruction speed was also improved. Our method achieves a better balance between memory size and computation time. Moreover, these compression methods can be applied to not only planar measurement environment but also cylindrical and spherical measurement environments. Additionally, our approach will naturally benefit from integrating compressed sensing methods [28], [46], [47]. A GPU accelerated [48] compressed sensing reconstruction method can also be expected to boost the calculation speed, because our method has the potential of high-performance parallel computation.

Although our proposed method can output better images, the artifacts are still distinct. Some limitations need to be resolved in order to obtain high-quality reconstruction images.

It affects the quality of PAT reconstruction how to compensate transducer properties, i.e., SIR related with element geometry and electromechanical response. Regarding element geometry, it was used to generate PAT signals based on a forward model. However, direct compensation of these transducer properties is not provided in this paper. We attempted to incorporate the compensation of SIR as the geometry of elements into the system matrix. In the simulation, SIR compensation achieved a significant improvement in the lateral resolution, while it did not demonstrate effective results in phantom experiment. We also conducted deconvolution techniques to compensate received PA signals by using the measured transducer's impulse response. However, the reconstructed images did not have distinct improvement. The main reason is that the central frequency (1 MHz) and bandwidth (70%) of the matrix probe are low, and consequently, the noise was not effectively suppressed. In the next study, a more effective deconvolution method and SIR compensation for transducer with wide bandwidth will be explored.

The model-based method basically requires a large amount of memory even if matrix compression is used. In some cases, this may be a limitation to the practical use of the model-based method. If the system matrix is explicitly stored, the memory complexity is approximately $O(n^3 n_x n_y n_s)$, where n is proportional to the voxel number in one side of the reconstruction region, n_x and n_y are the captured data in X- and Y-direction, respectively, and n_s is the sampling point number. If the system matrix is implicitly implemented, the computation time is not acceptable. Hence, the model-based method is hardly suitable to high-resolution PAT reconstruction. For example, when fine temporal sampling of high-frequency PA signals or wide area measuring with a small spatial sampling interval are required in order to avoid aliasing artifact [2], the system matrix size is apt to be larger than the computer's memory size. Hence, the model-based method is hardly suitable to the high resolution and large area PAT reconstruction. On the other hand, for our developed PA mammography (PAM) system, the objective is to provide an imaging tool for early breast cancer diagnosis based on the capillary vessel density of cancer. The spatial resolution of PAM is significantly restricted because of ultrasound attenuation caused by a large reconstruction range. Therefore, PAM is used to provide macroscopic vessel density instead of microscopic distribution. The results showed the proposed method attained enough spatial resolution to detect 0.3-mm wire targets, which is useful for our PAM system.

This study uses the CG method to solve the optimization problem, but in some cases this method converges to local minima. Therefore, regularization methods are usually adopted for computing a stable solution. We have investigated various penalty functions such as compressed sensing methods (e.g. L1–LS solver). When the problem size is small, the expected fast convergence rate and satisfactory reconstruction can be achieved. When the problem size increases, however, the convergence rate declines rapidly, and even an acceptable optimization result cannot be obtained. If nonlinear optimization methods are used, it is impossible to calculate the Jacobi matrix in a common computer. In this research, we confirmed that the CG method finally converges to the same solution for different initial values. In the future work, we will continue to research a better optimization method for solving the large-scale optimization problem.

Besides the aforementioned limitations, the sound speed heterogeneity also needs to be considered to improve the image quality. In other studies [18], [43]–[45], the sound speed heterogeneity can be resolved by compensating the sound speed during the reconstruction. In subsequent studies, an effective sound speed estimation method especially suitable for planar scanning PAT will be researched, and better reconstruction results are expected.

V. Conclusion

In this paper, we presented a fluence-compensation and reconstruction method for 3-D planar PAT. Light fluence compensation performed at each iteration, which minimizes the amplification of noise and artifacts. Furthermore, matrix compression methods made the proposed method applicable to 3-D reconstruction under planar measurement conditions, and the calculation speed was also accelerated. The simulation and phantom experiment results indicated that the proposed method reconstructs better quality images. We expect that the capability of increasing imaging depth will broaden clinical applications of PAT.

Acknowledgment

The authors would like to thank the anonymous reviewers for their valuable comments to improve this paper. The authors would also like to thank T. Nakajima and R. Nanaumi for helping to evaluate the optical properties of the phantom, and the team members of the Medical Imaging Project in Canon Inc. for the PA imaging system development.

REFERENCES

[1] C. Li and L. V. Wang, "Photoacoustic tomography and sensing in biomedicine," *Phys. Med. Biol.*, vol. 54, no. 19, pp. R59–R97, 2009.

[2] M. Xu and L. V. Wang, "Photoacoustic imaging in biomedicine," *Rev. Sci. Instrum.*, vol. 77, p. 041101, 2006.

[3] L. V. Wang and H.-i Wu, *Biomedical Optics: Principles and Imaging*. New York: Wiley, 2007.

[4] C. G. A. Hoelen and F. F. M. de Mul, "Image reconstruction for photoacoustic scanning of tissue structures," *Appl. Opt.*, vol. 39, no. 31, pp. 5872–5883, 2000.

[5] C. K. Liao, M. L. Li, and P. C. Li, "Optoacoustic imaging with improved synthetic focusing," *Proc. SPIE*, vol. 5697, pp. 255–262, 2005.

[6] S. Park, A. B. Karpiouk, S. R. Aglyamov, and S. Y. Emelianov, "Adaptive beamforming for photoacoustic imaging using linear array transducer," in *Proc. IEEE Ultrason. Symp.*, 2008, pp. 1088–1091.

[7] R. A. Kurger, P. Liu, Y. R. Fang, and C. R. Appledorn, "Photoacoustic ultrasound (PAUS)—Reconstruction tomography," *Med. Phys.*, vol. 22, no. 10, pp. 1605–1609, Oct. 1995.

[8] R. A. Kruger, D. R. Reinecke, and G. A. Kruger, "Thermoacoustic computed tomography—Technical considerations," *Med. Phys.*, vol. 26, no. 9, pp. 1832–1839, Sep. 1999.

[9] S. R. Deans, "The Randon transform and some of its applications," New York: Wiley.

[10] M. Xu and L. V. Wang, "Universal back-projection algorithm for photoacoustic computed tomography," *Phys. Rev. E*, vol. 71, no. 1, p. 016706, 2005.

[11] M. Xu and L. V. Wang, "Time-domain reconstruction for thermoacoustic tomography in a spherical geometry," *IEEE Trans. Med. Imag.*, vol. 21, no. 7, pp. 814–822, Jul. 2002.

[12] K. P. Kostli, D. Frauchiger, J. J. Niederhauser, G. Paltauf, H. P. Weber, and M. Frenz, "Optoacoustic imaging using a three-dimensional reconstruction algorithm," *IEEE J. Sel. Top. Quantum Electron.*, vol. 7, no. 6, pp. 918–923, Nov. 2001.

[13] Y. Xu, D. Feng, and L. V. Wang, "Extract frequency-domain reconstruction for thermoacoustic tomography—I: Planar geometry," *IEEE Trans. Med. Imag.*, vol. 21, no. 7, pp. 823–828, Jul. 2002.

[14] Y. Xu, D. Feng, and L. V. Wang, "Extract frequency-domain reconstruction for thermoacoustic tomography—II: Cylindrical geometry," *IEEE Trans. Med. Imag.*, vol. 21, no. 7, pp. 829–833, Jul. 2002.

[15] G. Paltauf, J. A. Viator, S. A. Prahl, and S. L. Jacques, "Iterative reconstruction algorithm for optoacoustic imaging," *J. Acoust. Soc. Amer.*, vol. 112, no. 4, pp. 1536–1544, 2002.

[16] J. Zhang, M. A. Anastasio, P. J. L. Riviere, and L. V. Wang, "Effects of different imaging models on least-squares image reconstruction accuracy in photoacoustic tomography," *IEEE. Trans. Med. Imag.*, vol. 28, no. 11, pp. 1781–1790, Nov. 2009.

[17] S. Ma, S. Yang, and H. Guo, "Limited-view photoacoustic imaging based on linear-array detection and filtered mean-backprojection-iterative reconstruction," *J. Appl. Phy.*, vol. 106, p. 123104, 2009.

[18] Z. Jing, W. Kun, Y. Yongyi, and A. A. Mark, "Simultaneous reconstruction of speed-of-sound and optical absorption properties in photoacoustic tomography via a time-domain iterative algorithm," *Proc. SPIE*, vol. 6856, p. 68561, 2008.

[19] A. Rosenthal, D. Razansky, and V. Ntziachristos, "Fast semi-analytical model-based acoustic inversion for quantitative optoacoustic tomography," *IEEE Trans. Med. Imag.*, vol. 29, no. 6, pp. 1275–1285, Jun. 2010.

[20] S. Bu, K. Kondo, M. Yamakawa, T. Shiina, K. Fukutani, Y. Someda, and Y. Asao, "Adaptive and quantitative reconstruction algorithm for photoacoustic tomography," in *Proc. SPIE*, vol. 7899, p. 78992G, 2011.

[21] K. Tanji, K. Watanabe, K. Fukutani, Y. Asao, T. Yagi, M. Yamakawa, and T. Shiina, "Advanced model-based reconstruction algorithm for practical three-dimensional photoacoustic imaging," in *Proc. SPIE*, vol. 7899, p. 78992K, 2011.

[22] M. L. Li, Y. C. Tseng, and C. C. Cheng, "Model-based correction of finite aperture effect in photoacoustic tomography," *Opt. Express*, vol. 18, no. 25, pp. 26285–26292, 2010.

[23] K. Wang, S. A. Ermilov, R. Su, H. P. Brecht, A. A. Oraevsky, and M. A. Anastasio, "An imaging model incorporating ultrasonic transducer properties for three-dimensional optoacoustic tomography," *IEEE Trans. Med. Imag.*, vol. 30, no. 2, pp. 203–214, Feb. 2011.

[24] B. T. Cox, S. R. Arridge, K. P. Kostli, and P. C. Beard, "Two-dimensional quantitative photoacoustic image reconstruction of absorption distribution in scattering media by use of a simple iterative method," *Appl. Opt.*, vol. 45, no. 8, pp. 1866–1875, 2006.

[25] Z. Yuan, Q. Wang, and H. Jiang, "Reconstruction of optical absorption coefficient maps of heterogeneous media by photoacoustic tomography coupled with diffusion equation based regularized Newton method," *Opt. Express*, vol. 15, no. 26, p. 18076, 2007.

[26] B. T. Cox, S. R. Arridge, and P. C. Beard, "Estimating chromophore distribution from multiwavelength photoacoustic images," *J. Opt. Soc. Amer.*, vol. 26, no. 2, p. 443, 2009.

[27] A. Rosenthal, D. Razansky, and V. Ntziachristos, "Quantitative optoacoustic signal extraction using sparse signal representation," *IEEE Trans. Med. Imag.*, vol. 28, no. 12, pp. 1997–2006, Dec. 2009.

[28] A. Rosenthal, D. Razansky, and V. Ntziachristos, "Sparse signal representation at the service of quantitative optoacoustic tomography," in *Proc. SPIE*, vol. 7564, p. 75640S, 2010.

[29] R. J. Zemp, "Quantitative photoacoustic tomography with multiple optical sources," *Appl. Opt.*, vol. 49, no. 18, p. 3566, 2010.

[30] P. Shao, B. Cox, and R. J. Zemp, "Estimating optical absorption, scattering, and Grueneisen distributions with multi-illumination photoacoustic tomography," *Appl. Opt.*, vol. 50, no. 19, p. 3145, 2011.

[31] P. M. Morse and K. U. Ingard, *Theoretical Acoustics*. Princeton, NJ: Princeton Univ. Press, 1987.

[32] G. J. Diebold, T. Sun, and M. I. Khan, "Photoacoustic monopole radiation in one, two, and three dimensions," *Phys. Rev. Lett.*, vol. 67, no. 24, pp. 3384–3387, 1991.

[33] L. H. Wang, S. L. Jacques, and L. Q. Zheng, "MCML - Monte Carlo modeling of photon transport in multi-layered tissues," *Comput. Methods Programs Biomed.*, vol. 47, pp. 131–146, 1995.

[34] S.R. Arridge, "Optical tomography in medical imaging," *Inverse Problems*, vol. 15, no. 2, p. R41, 1999.

[35] K. D. Paulsen and H. Jiang, "Spatially-varing optical property reconstruction using a finite element diffusion equation approximation," *Med. Phys.*, vol. 22, no. 6, pp. 619–701, 1995.

[36] C. G. A. Hoelen and F. F. M de Mul, "A new theoretical approach to photoacoustic signal generation," *J. Acoust. Soc. Amer.* vol. 106, no. 2, pp. 695–706 1999.

[37] M. W. Sigrist and F. K. Kneubuhl, "Laser generated stress waves in liquids," *J. Acoust. Soc. Amer.* vol. 64, pp. 1652–1663, 1978.

[38] B. Piwakowski and K. Sbai, "A new approach to calculate the field radiated from arbitrarily structured transducer array," *IEEE Trans. Ultra. Ferr. Freq. Con.*, vol. 46, no. 2, pp. 422–440, Mar. 1999.

[39] K. Fukutani, Y. Someda, M. Taku, Y. Asao, S. Kobayashi, T. Yagi, M. Yamakawa, T. Shiina, T. Sugie, and M. Toi, "Characterization of photoacoustic tomography system with dual illumination modes," in *Proc. SPIE*, 2011, vol. 7899, p. 78992J.

[40] E. F. D. Azevedo, M. R. Fahey, and R. T. Mills, "Vectorized sparse matrix multiply for compressed row storage format," in *Proc. Int. Conf. Comput. Sci.*, 2005, vol. 3514, pp. 99–106.

[41] A. Q. Bauer, R. E. Nothdurft, C. Li, L. V. Wang, and J. P. Culver, "Correcting for heterogeneous fluence profiles in photoacoustic imaging with diffuse optical tomography," presented at the Biomed. Opt., Miami, FL, 2010.

[42] C. Xu, P. D. Kumavor, A. Aguirre, and Q. Zhu, "Investigation of DOT-assisted photoacoustic tomography in reflection geometry," in *Proc. SPIE*, vol. 7899, p. 78990U, 2011.

[43] M. A. Anastasio, J. Zhang, X. Pan, Y. Zhou, G. Ku, and L. V. Wang, "Half-time image reconstruction in thermoacoustic tomography," *IEEE. Trans. Med. Imag.*, vol. 24, no. 2, pp. 199–210, Feb. 2005.

[44] H. Jiang, Z. Yuan, and X. Gu, "Spatially varying optical and acoustic property reconstruction using finite-element-based photoacoustic tomography," *J. Opt. Amer. A*, vol. 23, no. 4, pp. 878–888, 2006.

[45] J. Jose, R. G. H. Willemink, S. Resink, D. Piras, J. C. G. van Hespen, C. H. Slump, W. Steenbergen, T. G. van Leeuwen, and S. Manohar, "Passive element enriched photoacoustic computed tomography (PER PACT) for simultaneous imaging of acoustic propagation properties and light absorption," *Opt. Express*, vol. 19, no. 3, pp. 2093–2104, 2011.

[46] J. Provost and F. Lesage, "The application of compressed sensing for photo-acoustic tomography," *IEEE. Trans. Med. Imaging*, vol. 28, no. 4, pp. 585–594, Apr. 2009.

[47] Z. Guo, C. Li, L. Song, and L. V. Wang, "Compressed sensing in photoacoustic tomography *in vivo*," *J. Bio. Opt.*, vol. 15, no. 2, p. 021311, 2010.

[48] M. M. Baskaram and R. Bordawekar, "Optimizing sparse matrix-vector multiplication on GPUs," IBM, Armonk, NY, Tech. Rep. RC24704, 2008.

Authors' photographs and biographies not available at the time of publication.